



## City Research Online

### City, University of London Institutional Repository

---

**Citation:** Degtyarev, V. & Tsavdaridis, K. D. (2022). Buckling and ultimate load prediction models for perforated steel beams using machine learning algorithms. *Journal of Building Engineering*, 51, 104316. doi: 10.1016/j.jobe.2022.104316

This is the accepted version of the paper.

This version of the publication may differ from the final published version.

---

**Permanent repository link:** <https://openaccess.city.ac.uk/id/eprint/27946/>

**Link to published version:** <https://doi.org/10.1016/j.jobe.2022.104316>

**Copyright:** City Research Online aims to make research outputs of City, University of London available to a wider audience. Copyright and Moral Rights remain with the author(s) and/or copyright holders. URLs from City Research Online may be freely distributed and linked to.

**Reuse:** Copies of full items can be used for personal research or study, educational, or not-for-profit purposes without prior permission or charge. Provided that the authors, title and full bibliographic details are credited, a hyperlink and/or URL is given for the original metadata page and the content is not changed in any way.

---

---

---

City Research Online:

<http://openaccess.city.ac.uk/>

[publications@city.ac.uk](mailto:publications@city.ac.uk)

---

# Buckling and ultimate load prediction models for perforated steel beams using machine learning algorithms

Vitaliy V. Degtyarev<sup>a,\*</sup>, Konstantinos Daniel Tsavdaridis<sup>b</sup>

<sup>a</sup>*New Millennium Building Systems, LLC, 3700 Forest Dr. Suite 501, Columbia, SC 29204, USA*

<sup>b</sup>*Department of Civil Engineering, School of Mathematics, Computer Science and Engineering, City, University of London, Northampton Square, London EC1V 0HB, UK*

---

## Abstract

Large web openings introduce complex structural behaviors and additional failure modes of steel cellular beams, which must be considered in the design using laborious calculations (e.g., exercising SCI P355). This paper presents seven machine learning (ML) models, including decision tree (DT), random forest (RF), k-nearest neighbor (KNN), gradient boosting regressor (GBR), extreme gradient boosting (XGBoost), light gradient boosting machine (LightGBM), and gradient boosting with categorical features support (CatBoost), for predicting the elastic buckling and ultimate loads of steel cellular beams. Large datasets of finite element (FE) simulation results, validated against experimental data, were used to develop the models. The ML models were fine-tuned via an extensive hyperparameter search to obtain their best performance. The elastic buckling and ultimate loads predicted by the optimized ML models demonstrated excellent agreement with the numerical data. The accuracy of the ultimate load predictions by the ML models exceeded the accuracy provided by the existing design provisions for steel cellular beams published in SCI P355 and AISC De-

---

\*Corresponding author

*Email addresses:* [vitaliy.degtyarev@newmill.com](mailto:vitaliy.degtyarev@newmill.com), [vitdegtyarev@yahoo.com](mailto:vitdegtyarev@yahoo.com) (Vitaliy V. Degtyarev), [konstantinos.tsavdaridis@city.ac.uk](mailto:konstantinos.tsavdaridis@city.ac.uk) (Konstantinos Daniel Tsavdaridis)

sign Guide 31. The relative feature importance and feature dependence of the models were evaluated and discussed in the paper. An interactive Python-based notebook and a user-friendly web application for predicting the elastic buckling and ultimate loads of steel cellular beams using the developed optimized ML models were created and made publicly available. The web application deployed to the cloud allows for making predictions in any web browser on any device, including mobile. The source code of the application available on GitHub allows running the application locally and independently from the cloud service.

*Keywords:* Cellular beams, Perforated web, Elastic buckling, Ultimate strength, Predictive models, Machine learning

---

## 1. Introduction

Perforated steel beams with repeating web openings have been used in construction for more than a century [1]. They offer several advantages over steel beams with solid webs, including weight reduction, higher strength-to-weight ratio, integration of utilities, and improved aesthetics. Castellated beams with hexagonal openings, which were the first type of beams with perforated web sections, have practically been replaced in modern construction by cellular beams with circular openings [2]. Multiple large openings cause a significant reduction in the beam shear strength and introduce additional possible failure modes of the beams, which makes the flexural behavior and design of cellular beams complicated. A cellular beam may exhibit one of the following failure modes: global bending, lateral-torsional buckling, vertical shear, local Vierendeel bending, web post horizontal shear, web post bending, web post buckling, and shear buckling. Many researchers have contributed to the body of knowledge about the strength and structural behavior of steel cellular beams. Several research publications describe numerical studies on the lateral-torsional buckling of cellular beams [3–8], which allowed for determining the effects of different design

18 parameters on the beam strength governed by the elastic and inelastic lateral-  
19 torsional buckling. It was found in particular that the cellular beam geometry  
20 affected the moment-gradient coefficient, which is not the case for the solid-web  
21 beams [4]. T-shaped stiffeners were proposed to improve the flexural stiffness of  
22 cellular beams and reduce the lateral-torsional buckling occurrence [5]. Modi-  
23 fied calculations of the cross-sectional properties and a modified buckling curve  
24 selection were developed based on the existing European guidelines [6].

25 Web post buckling of cellular beams and beams with web openings of dif-  
26 ferent shapes was studied in [9–11]. Tsavdaridis and D’Mello [9] demonstrated  
27 that particular non-standard opening shapes improved the beam structural per-  
28 formance compared with the beams with standard circular, hexagonal, and elon-  
29 gated web openings. They also proposed an empirical formula for predicting the  
30 ultimate vertical shear strength of web posts formed by the different opening  
31 shapes. Panedpojaman et al. [10] proposed design equations for predicting the  
32 shear strength of local web post buckling in symmetric and asymmetric cellular  
33 beams, which demonstrated improved accuracy in predicting the shear strength  
34 compared with BS EN 1993-1-1 [12] and AISC 360 [13].

35 Chung et al. [14] investigated the Vierendeel mechanism in cellular steel  
36 beams and found that shear yielding is more critical in steel beams with cir-  
37 cular openings than in beams with rectangular openings. They proposed an  
38 empirical shear moment interaction curve at the perforated sections. Kang et  
39 al. [15] studied the shear behavior and strength of cellular beams and proposed  
40 a rational design model for predicting the beam shear strength, which showed a  
41 good agreement with the numerical and experimental results. Ellobody [16] in-  
42 vestigated combined buckling modes of steel cellular beams and found that the  
43 failure load could be significantly reduced when the beams failed in combined  
44 web distortional and web post-buckling.

45 Several research papers have been dedicated to the optimal design of cellular  
46 beams [9, 17–24]. The studies demonstrated that the strength and weight of  
47 the beams with web openings could be significantly improved by using non-  
48 standard opening shapes [9, 17, 19, 21], applying special optimization techniques  
49 [18, 20, 22], and selecting specific sizes and spacing of web openings [21, 23, 24].

50 Akrami and Erfani [25] assessed design methodologies for perforated steel  
51 beams presented in ASCE 23-97 [26], SCI P100 [27], SCI P355 [2], Chung et  
52 al. [28], and Tsavdaridis and D’Mello [17]. The two latter methods were found  
53 least restrictive and produced the lowest errors. The authors proposed ASCE  
54 23-97 modifications, which showed a good agreement with experimental and  
55 numerical data.

56 The presented literature review shows that the published research concen-  
57 trated mainly on studying specific failure modes of cellular beams. To fill the  
58 gap in the information about the global response of such members, Rajana et al.  
59 [29] performed an extensive numerical parametric study of the elastic and inelas-  
60 tic buckling of cellular beams subjected to strong axis bending. The effects of  
61 various parameters on the elastic buckling and ultimate loads of cellular beams  
62 were investigated, and an extensive database of the FE simulation results was  
63 generated. The study showed that the elastic buckling was affected mainly by  
64 the web thickness and the flange geometry. The diameter of web openings, their  
65 spacing, flange geometry, and web thickness were the most critical parameters  
66 affecting the beam strength. It was also determined that the initial geometric  
67 imperfections had an insignificant effect on the predicted beam strength.

68 Artificial intelligence (AI) and machine learning (ML) are emerging fields  
69 of computer science that allow for developing machines with simulated human  
70 intelligence and creating data-based descriptive models capable of handling very  
71 complex problems efficiently. A properly developed ML model for engineering

72 applications reveals hidden relations between the predicted variable and input  
73 parameters based on the underlying physics. Many industries have successfully  
74 adopted AI and ML [30–33], whereas their deployment in structural engineering  
75 is still somewhat limited despite many research publications demonstrating the  
76 accuracy and effectiveness of the AI and ML methods.

77 The number of research publications on ML applications in civil and struc-  
78 tural engineering had increased exponentially since the second half of the 1980s,  
79 when the first papers on this topic were published [34–40]. Many publica-  
80 tions described ML models considered in this study for predicting properties  
81 of concrete and reinforced concrete structures [41–66]. Fewer papers have been  
82 published on ML applications to steel structures, including buckling analysis of  
83 beam-columns [67], cold-formed steel (CFS) space structure optimization [68],  
84 web crippling strength prediction [69], elastic distortional buckling stress de-  
85 termination [70, 71], rotation capacity prediction [72], strength prediction of  
86 concrete-filled steel tubular columns [73], failure mode identification of column  
87 base plate connection [74], capacity prediction of cold-formed stainless steel  
88 tubular columns [75], seismic drift demand estimation for steel moment frame  
89 buildings [76], and shear strength of CFS channels with staggered perforated  
90 webs [77–80]. ML techniques were previously applied to steel cellular beams.  
91 Sharifi et al. [81] developed an artificial neural network (ANN) to predict the  
92 flexural strength of steel cellular beams governed by lateral-torsional buckling  
93 using a relatively small dataset with 99 samples. The predicting abilities of  
94 the developed ANN were superior to those by the Australian Standard [82].  
95 Abambres et al. [83] developed an ANN model and an ANN-based formula for  
96 predicting the elastic buckling load of cellular beams using a large dataset of  
97 numerical results described in [29]. The ANN and the proposed formula showed  
98 an excellent agreement with the FE simulation results. An ANN and ANN-

99 based formula for predicting the lateral-torsional buckling resistance of slender  
100 steel cellular beams were presented by Ferreira et al. [84]. Limbachiya and  
101 Shamass [85] presented an ANN and ANN-based formula for predicting web-  
102 post buckling shear strength of cellular beams, which demonstrated a higher  
103 level accuracy compared with the existing design provisions.

104 The presented review indicates that ML has excellent potential for develop-  
105 ing structural engineering expert tools. ML models cannot currently be solely  
106 used for final designs because building codes do not permit them. However,  
107 they can be employed in the preliminary design stages to quickly evaluate and  
108 select options that may work and consider them in the detailed analysis and  
109 design per building codes. Due to the superior performance of ML models com-  
110 pared with conventional models demonstrated on many engineering problems,  
111 the question of what should be done to adopt them in building codes will need  
112 to be eventually answered. ML models are based on solid mathematical algo-  
113 rithms, well-described in the literature. The novelty of the algorithms, which  
114 structural engineers do not fully understand, is one of the significant barriers  
115 today to their adoption, which will eventually change with more education,  
116 research, and experience.

117 ML models built on top of the available test or numerical data are compu-  
118 tationally efficient and often more accurate than the existing design methods  
119 based on the traditional approaches, which often rely on fewer data points and  
120 engineering intuition. They can replace computationally intensive finite element  
121 simulations when the design parameters are within the ranges of the data used  
122 for the ML model training. It should also be noted that accurate finite element  
123 simulations require advanced software resources, which are not always available  
124 to designers, and advanced techniques, thus skills and knowledge. Even when  
125 the appropriate software is available, and the designers possess the required ex-

126 pertise, it is impractical to perform advanced finite element simulations during  
127 the project design phase due to time constraints. Because of that, engineers are  
128 often using simplified FEA to perform stress analyses. The downside is that  
129 these are not very accurate due to the number of assumptions, leading to the  
130 very same initial problem: the need of higher safety factors and the excessive  
131 use of material where it is not needed.

132 This study aims to explore various ML algorithms for predicting the elastic  
133 buckling and ultimate loads of steel cellular beams. Considering the complexity  
134 of the structural behavior and design of such members, ML models are deemed to  
135 be a promising alternative to the existing design guidelines and computationally  
136 expensive FE modeling. The objectives of the study were as follows:

- 137 1. Develop and optimize ML models for predicting the elastic buckling and ul-  
138 timate loads of steel cellular beams based on seven popular ML regressors,  
139 including decision tree (DT), random forest (RF), k-nearest neighbors  
140 (KNN), gradient boosting regressor (GBR), extreme gradient boosting  
141 (XGBoost), light gradient boosting machine (LightGBM), and gradient  
142 boosting with categorical features support (CatBoost).
- 143 2. Interpret and explain the developed models using the permutations and  
144 SHapley Additive exPlanations (SHAP) [86] methods.
- 145 3. Compare predictions by the developed ML models with those per SCI  
146 P355 [2] and AISC Design Guide 31 [87].

147 ML models were trained using FE simulation results of steel cellular beams  
148 published in [29]. The elastic buckling load dataset included 3645 samples. The  
149 ultimate load (inelastic buckling load) dataset consisted of 78390 samples. All  
150 models were implemented in open-source Python-based frameworks, and their  
151 hyperparameters were optimized via an extensive tuning process. The ten-fold  
152 cross-validation method was employed for the model training and performance

153 evaluation. The final evaluation of the models was performed on the data unseen  
154 by the models during training. The ML model predictions showed an excellent  
155 agreement with the FE simulation results. The ultimate loads of the cellular  
156 beams predicted by the models compared with the FE analysis data considerably  
157 better than the ultimate loads predicted by SCI P355 [2] and AISC Design Guide  
158 31 [87]. The developed ML models allow for computing the elastic buckling  
159 and ultimate loads of cellular beams with a wide range of variables, including  
160 intermediate values of variables not considered in numerical studies used for the  
161 model training.

162 A web application for predicting the elastic buckling and ultimate loads of  
163 steel cellular beams was created in Streamlit. A light version of the application  
164 was deployed to the cloud at <https://scba-cb.herokuapp.com/>. It allows for  
165 making predictions in any web browser on any device, including mobile. The  
166 source codes of the full and lite application versions are available on GitHub  
167 at <https://github.com/vitdegyarev/SCBA-Streamlit> and <https://github.com/vitdegyarev/SCBA-Streamlit-CB>, respectively. They allow for  
168 running the application on a local machine. The scientific research part of this  
169 study consists of creating and optimizing ML models for predicting the behavior  
170 of cellular beams, while the web application is a convenient tool for obtaining  
171 predictions by the developed models.

173 The novelty of the presented work consists of the development of new opti-  
174 mized ML models for accurate and computationally efficient predictions of the  
175 elastic buckling and ultimate loads of steel cellular beams, interpretation and ex-  
176 planation of the developed models using the permutations and SHAP methods,  
177 comparison of the performance of seven different ML models, and development  
178 of a web application based on the optimized ML models for the ease of use by  
179 engineers in practice.

180 **2. Datasets**

181 The elastic buckling load,  $w_{cr}$ , and ultimate load (inelastic buckling load),  
 182  $w_{max}$ , datasets of FE simulation results from [29] were used for training and per-  
 183 formance evaluation of the ML models. The FE models were validated against  
 184 the experimental data, as described in [29]. The  $w_{cr}$  and  $w_{max}$  datasets consist  
 185 of 3645 and 78390 samples, respectively. Fig. 1 shows dimensional parameters  
 186 of the cellular beams considered in the numerical parametric study, including  
 187 beam span length,  $L$ ; beam height,  $H$ ; flange width,  $b_f$ ; flange thickness,  $t_f$ ;  
 188 web thickness,  $t_w$ ; opening diameter,  $D_o$ ; web post width,  $WP$ ; and opening  
 189 end distance,  $L_{ed}$ .

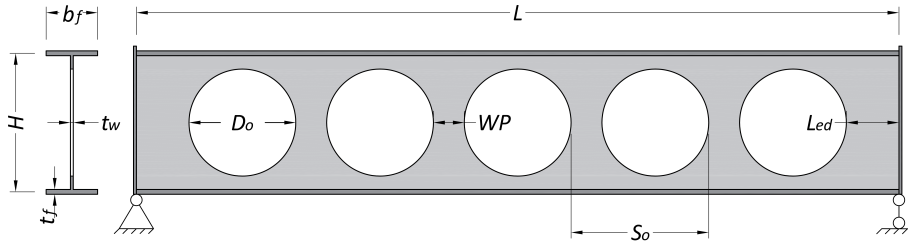


Figure 1: Dimensional parameters of steel cellular beams

190 In addition to the dimensional parameters of the beams, the ultimate load  
 191 dataset included steel yield stress,  $F_y$ ; steel ultimate stress,  $F_u$ ; steel yield strain,  
 192  $\epsilon_y$ ; steel ultimate strain,  $\epsilon_u$ ; and initial geometric imperfections considered in  
 193 the FE models. The dimensional beam characteristics shown in Fig. 1 and  $F_y$   
 194 (in the  $w_{max}$  models only) were considered the ML models' input parameters.  
 195 The initial geometric imperfections were excluded from the input parameters  
 196 because they have an insignificant effect on  $w_{max}$  [29], and their exact shape  
 197 and magnitude are not usually known to the designer.

198 Distributions of the parameters in the elastic buckling and ultimate load  
 199 datasets presented in Figs. 2 and 3 demonstrate that the datasets cover a wide

200 range of the beams and represent the steel cellular beams used in construction.

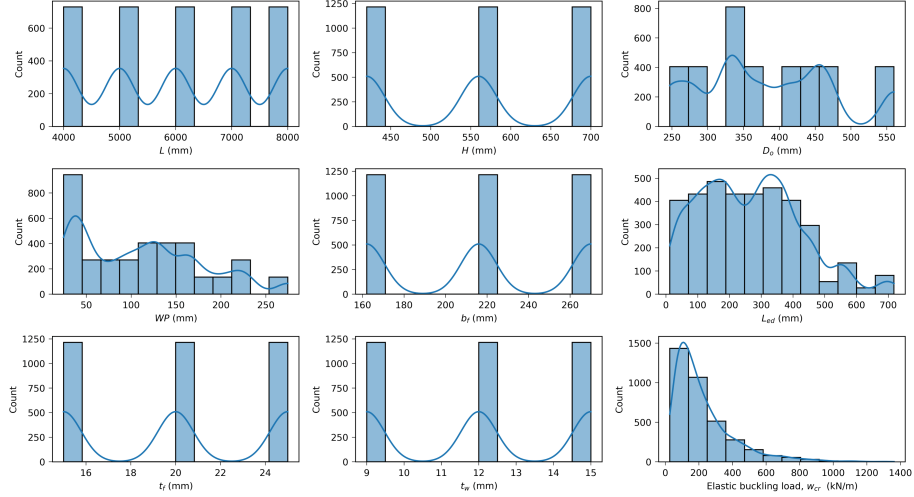


Figure 2: Distributions of variables of the elastic buckling load dataset

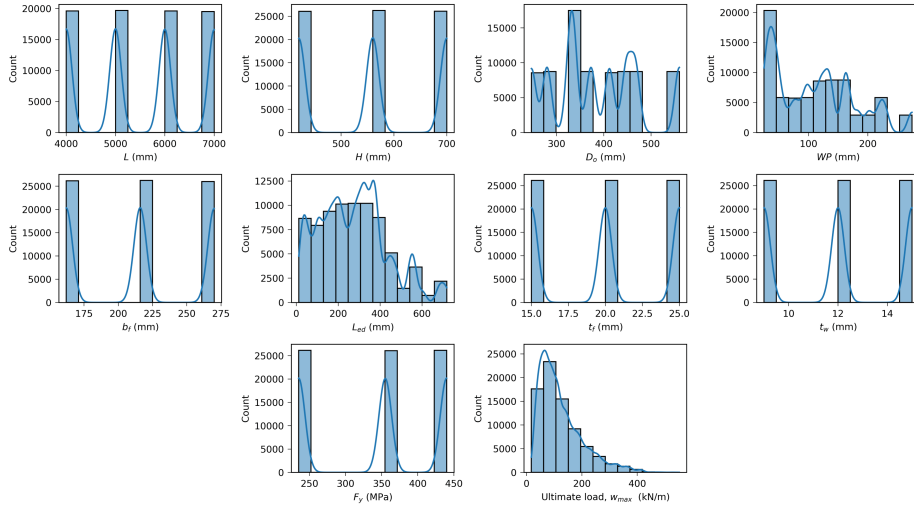


Figure 3: Distributions of variables of the ultimate load dataset

201 Fig. 4 and 5 show correlation matrices for the dataset variables. The beam  
 202 span length,  $L$ , has the highest negative correlation with  $w_{cr}$  and  $w_{max}$ , char-  
 203 acterized by moderate coefficients of correlation of  $-0.67$  and  $-0.60$ , respectively.

204 All other variables have weak correlations with  $w_{cr}$  and  $w_{max}$ , with coefficients  
 205 of correlation not exceeding 0.37. It is interesting to note that  $w_{max}$  has a con-  
 206 siderably stronger correlation with  $WP$  than  $w_{cr}$ , which indirectly highlights  
 207 the positive contribution of the web post plastic behavior to the ultimate load  
 208 of the cellular beams.  $D_o$  has a strong positive correlation with  $H$  because the  
 209  $D_o$  values were set as fractions of the  $H$  values in the numerical parametric  
 210 study. All other dataset variables have weak correlations between themselves.

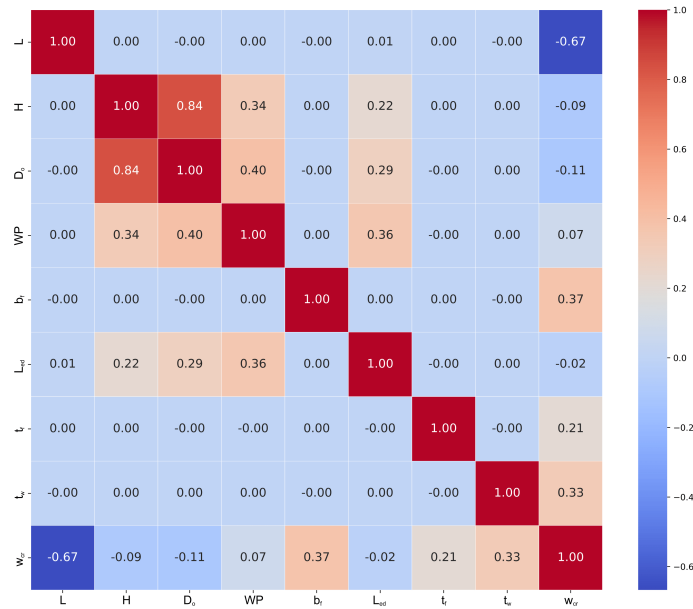


Figure 4: Correlation matrix for the elastic buckling load dataset

211 The datasets used in this study can be found at the following link: <https://www.kaggle.com/vitdegyarev/buckling-and-ultimate-loads-of-cellular-beams>.  
 212  
 213

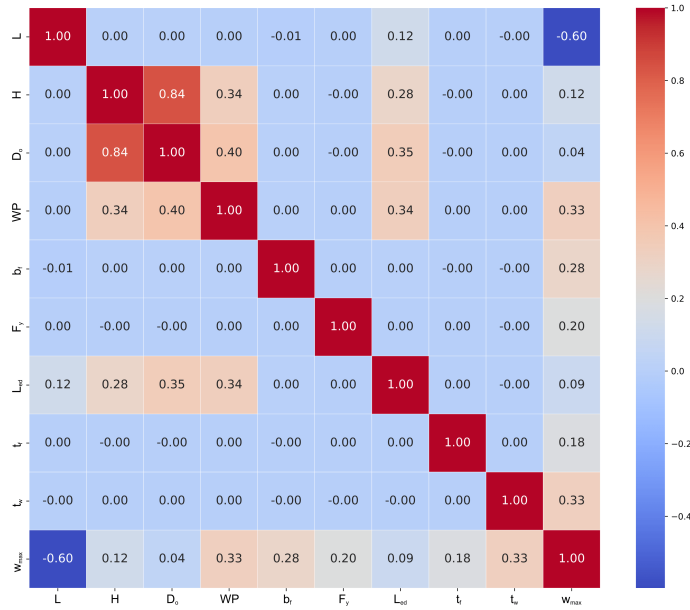


Figure 5: Correlation matrix for the ultimate load dataset

### 214 3. Review of machine learning algorithms

215 The abilities of seven popular supervised ML algorithms to predict the elas-  
 216 tic buckling load,  $w_{cr}$ , and ultimate load,  $w_{max}$ , of steel cellular beams were  
 217 evaluated. Supervised ML algorithms learn by example using labeled train-  
 218 ing data, which consist of input parameters (also known as features) and one  
 219 or more output values (also known as targets). The evaluated ML algorithms  
 220 included decision tree (DT), random forest (RF), k-nearest neighbors (KNN),  
 221 gradient boosting regressor (GBR), extreme gradient boosting (XGBoost), light  
 222 gradient boosting machine (LightGBM), and gradient boosting with categorical  
 223 features support (CatBoost). These algorithms are commonly employed to de-  
 224 velop predictive ML models in civil/structural engineering (as was discussed in  
 225 the Introduction section) and other domains. They are based on different princi-  
 226 ples and may result in different performances when used for different problems.  
 227 One algorithm may demonstrate a better predictive accuracy than others on

228 one problem and inferior performance on a different problem. Therefore, it is  
 229 important to find an algorithm and its optimal hyperparameters that works the  
 230 best for a given problem.

231 Fig. 6 demonstrates the schematic architecture of the considered ML models  
 232 for predicting  $w_{cr}$  and  $w_{max}$ . The models consisted of features, ML algorithms,  
 233 and targets. The features of the models for predicting  $w_{cr}$  were  $L$ ,  $H$ ,  $b_f$ ,  $t_f$ ,  
 234  $t_w$ ,  $D_o$ ,  $WP$ , and  $L_{ed}$ . The  $w_{max}$  models also included  $F_y$  as a feature.

235 All ML algorithms have hyperparameters, or the parameters specified before  
 236 the model training to control the learning process and avoid overfitting or un-  
 237 derfitting. Overfitting is characterized by the ability of a model to make good  
 238 predictions for the samples used in training while making poor predictions on  
 239 the new samples of data unseen by the model before. An underfitted model  
 240 produces poor predictions on the seen and unseen data. The ability of an ML  
 241 model to make good predictions for previously unseen data is referred to as gen-  
 242 eralization. Finding optimal hyperparameters is essential for obtaining a model  
 243 with the best performance and generalization [54, 77]. It is equivalent to finding  
 244 the form and coefficients of a regression equation that gives the best prediction  
 245 accuracy for a given problem.

246 The following sections present a brief overview of each ML algorithm con-  
 247 sidered in the study. Detailed information about the ML algorithms and their  
 248 practical implementation can be found in published literature, including [88]  
 249 and [89].

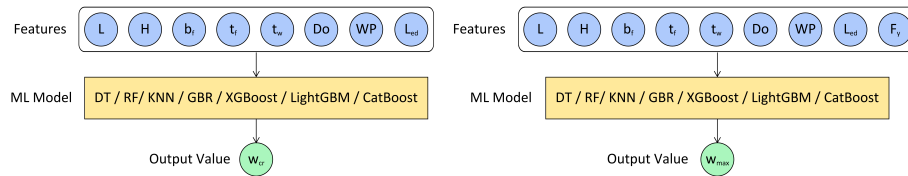


Figure 6: Architecture of ML models

250 *3.1. Decision tree*

251 The DT algorithm bears its name from its tree structure incrementally de-  
 252 veloped by splitting the dataset into smaller subsets. DT models have three  
 253 types of nodes: root node, decision nodes, and terminal nodes (also known as  
 254 leaves). The learning starts at the root node, which includes all training data.  
 255 The root node splits into two or more decision nodes, which include subsets of  
 256 the original training data. The splitting occurs based on a series of questions  
 257 determined by the algorithm. It continues for the subsequent levels until a pre-  
 258 defined maximum depth of the tree is reached or when the nodes have only one  
 259 sample of the training data. The algorithm stops at the terminal nodes, which  
 260 do not split.

Various algorithms for growing a DT exist. They differ by the possible tree structure, the split finding criteria, the splitting stoppage criteria, and the model estimation within the terminal nodes. The classification and regression trees (CART) algorithm [88] was used in this study. In this algorithm, a dataset  $(x_i, y_i)$  for  $i = 1, 2, \dots, N$ , with  $x_i = (x_{i1}, x_{i2}, \dots, x_{ip})$  is considered, where  $x_i$  and  $y_i$  are features and targets,  $N$  is the number of samples, and  $p$  is the number of features. The original dataset is split into  $M$  regions  $R_1, R_2, \dots, R_M$ . The model prediction in each region is a constant  $c_m$  described by Eq. 1.

$$f(x) = \sum_{m=1}^M c_m I(x \in R_m) \quad (1)$$

261 where  $I(x \in R_m)$  is the identity function that returns 1 if  $x$  is in the subset  $R_m$   
 262 and 0 otherwise.

The best  $\hat{c}_m$  is the average of  $y_i$  in region  $R_m$  when the sum of squared errors  $\sum(y_i - f(x_i))^2$  is used as the criterion of minimization:

$$\hat{c}_m = \text{ave}(y_i \mid x_i \in R_m) \quad (2)$$

263 The following greedy algorithm is employed to find the best binary partition  
 264 of each node in terms of the minimum sum of squared errors. The pair of  
 265 half-planes partitioned by a splitting variable  $j$  and a split point  $s$  is defined as  
 266 follows.

$$R_1(j, s) = \{X \mid X_j \leq s\} \text{ and } R_2(j, s) = \{X \mid X_j > s\} \quad (3)$$

267 The splitting variable  $j$  and the split point  $s$  that solve Eq. (4) are sought.

$$\min_{j,s} \left[ \min_{c_1} \sum_{x_i \in R_1(j,s)} (y_i - c_1)^2 + \min_{c_2} \sum_{x_i \in R_2(j,s)} (y_i - c_2)^2 \right] \quad (4)$$

268 The inner minimization is solved by

$$\hat{c}_1 = \text{ave}(y_i \mid x_i \in R_1(j, s)) \text{ and } \hat{c}_2 = \text{ave}(y_i \mid x_i \in R_2(j, s)) \quad (5)$$

269 Once the best split is found, the dataset is partitioned into two resulting  
 270 subsets, after which the splitting process is repeated for each subset and each  
 271 node in the subsequent levels.

272 The DT advantages consist of the relative ease of data preparation, the ease  
 273 of understanding and interpretation, and robustness against missing values. One  
 274 of the main disadvantages of DT is their proneness to overfitting when the tree  
 275 is very large [90, 91]. To avoid overfitting, the DT model should not be very  
 276 large. At the same time, the model should be large enough to capture the  
 277 important relationships between the features and targets to avoid underfitting.  
 278 DT hyperparameters include the maximum depth of the tree, the minimum  
 279 number of samples required to split an internal node, the minimum number of  
 280 samples required to be at a leaf node, and others.

281 *3.2. Random forest*

282 RF is an ensemble of DTs generally trained via *bagging*, which stands for  
283 *bootstrap aggregating* [88]. In this method, the same algorithm (DT) is trained  
284 many times on different random subsets of the entire training set. The sampling  
285 is performed with replacement, meaning that the same sample may appear  
286 in different subsets. Predictions from multiple randomly generated DTs are  
287 averaged to obtain the final output value of the RF algorithm.

288 The RF regression algorithm consists of the following steps [88].

289 1. For  $b=1$  to  $B$ , where  $b$  is an individual DT and  $B$  is the total number of  
290 DTs (estimators):

- 291 (a) A bootstrap sample of size  $N$  is drawn from the training data.
- 292 (b) A tree  $T_b$  is grown to the bootstrapped data by repeating the fol-  
293 lowing substeps for each node until the maximum tree depth or the  
294 minimum node size is reached:
  - 295 i.  $m$  variables are randomly selected from  $p$  variables.
  - 296 ii. The best variable among  $m$  and the best split point is found.
  - 297 iii. The node is split into two nodes.

298 2. The ensemble of trees  $\{T_b\}_1^B$  is output.

299 3. The final prediction is made as  $\hat{f}_{RF}^B(x) = \frac{1}{B} \sum_{b=1}^B T_b(x)$ .

300 The RF advantages include those listed in Subsection 3.1 for DT and its  
301 robustness against overfitting due to the presence of multiple independent DTs  
302 making predictions. On the negative side, RF requires more computational  
303 power and resources to build numerous trees and combine their outputs com-  
304 pared with DT. The RF hyperparameters include those for DTs plus the number  
305 of trees in the forest.

306 *3.3. K-nearest neighbors*

307 The KNN regression algorithm predicts the output value by interpolating  
 308 the output values of  $k$  nearest neighbors in the training set. The number of  
 309 neighbors  $k$  is a hyperparameter set before training. The distance between the  
 310 neighbors is defined by the distance function in the form of the Minkowski metric  
 311 described by Eq. (6). The Euclidean and Manhattan distances, which are other  
 312 typical distance metrics, can be obtained from the Minkowski metric by setting  
 313 the power parameter,  $p$ , equal to 1 and 2, respectively.

$$D(X, Y) = \left( \sum_{i=1}^k |x_i - y_i|^p \right)^{\frac{1}{p}} \quad (6)$$

The output values are obtained by taking either an average (Eq.(7)) or an inverse distance weighted average (Eq.(8)) of the  $k$  nearest neighbors with similar features. In the latter approach, closer neighbors have a more significant influence on the target than the more distant neighbors.

$$\hat{f}(x) = \frac{1}{k} \sum_{x_i \in N_k(x)} y_i \quad (7)$$

$$\hat{f}(x) = \frac{\sum_{x_i \in N_k(x)} \frac{1}{d_i} y_i}{\sum_{x_i \in N_k(x)} \frac{1}{d_i}} \quad (8)$$

314 where  $N_k(x)$  is the neighborhood of  $x$  defined by the  $k$  closest points  $x_i$  in the  
 315 training data,  $d_i$  is the distance from the  $i^{th}$  point to the estimated point.

316 The KNN advantages include the ease of implementation, the ability to  
 317 add new data without the effect on the algorithm's accuracy, and the training  
 318 period absence, which makes the KNN algorithm significantly faster than other  
 319 ML algorithms when the dataset size and the number of input variables are  
 320 relatively small. The KNN disadvantages consist of sensitivity to noisy data,  
 321 missing values and outliers, and slow predictions for large datasets and datasets

322 with a large number of features. The KNN hyperparameters are the number of  
 323 neighbors, the weight function (uniform or inverse distance weighted), and the  
 324 distance metric.

### 325 3.4. Gradient boosting

326 Boosting algorithms, or boosting machines, are ensemble methods that com-  
 327 bine several weak learners (usually DTs) to produce a strong learner. Boosting  
 328 machine predictors are trained sequentially, with each subsequent learner im-  
 329 proving the predecessor’s predictions. The algorithm stops when a predefined  
 330 number of predictors is reached or when the perfect fit is achieved. The two  
 331 common boosting algorithms are gradient boosting and adaptive boosting.

332 In gradient boosting, the boosting algorithm is combined with gradient de-  
 333 scent, which is an iterative optimization algorithm for finding a local minimum  
 334 of a function. New predictors are fitted to the residual errors from the previous  
 335 predictors. The gradient boosting algorithm includes the following steps [92]:

- 336 1. For a training set  $(x_i, y_i)_{i=1}^n$ , the model is initialized with a constant value  
 337 of

$$F_0(x) = \underset{\gamma}{\operatorname{argmin}} \sum_{i=1}^n L(y_i, \gamma) \quad (9)$$

338 where  $i$  and  $n$  denote the  $i^{\text{th}}$  sample and the total number of samples

- 339 2. For  $m=1$  to  $M$ , where  $m$  and  $M$  are the  $m^{\text{th}}$  iteration and the total number  
 340 of iterations:

- 341 (a) Pseudo-residuals are computed as follows:

$$r_{im} = - \left[ \frac{\partial L(y_i, F(x_i))}{\partial F(x_i)} \right]_{F(x)=F_{m-1}(x)} \quad (10)$$

- 342 (b) The training set  $(x_i, r_{im})_{i=1}^n$  is used to fit a predictor  $h_m(x)$  to  
 343 pseudo-residuals.

344 (c) Multiplier  $\gamma_m$  is computed by solving the following optimization prob-  
345 lem:

$$\gamma_m = \underset{\gamma}{\operatorname{argmin}} \sum_{i=1}^n L[y_i, F_{m-1}(x_i) + \gamma h_m(x_i)] \quad (11)$$

346 (d) The model is updated using the following equation:

$$F_m(x) = F_{m-1}(x) + \gamma_m h_m(x) \quad (12)$$

347 3.  $F_M(x)$  is obtained.

348 The gradient boosting algorithm’s advantages include high accuracy, flexi-  
349 bility, and the ability to handle missing data. It is generally considered resistant  
350 to overfitting due to many weak learners involved in the prediction. However,  
351 the algorithm may overfit when its hyperparameters are poorly selected. The  
352 disadvantages of gradient boosting are computation cost, the number of hyper-  
353 parameters that require proper tuning, and limited interpretability.

354 The gradient boosting hyperparameters include learning rate, the number of  
355 boosting iterations, maximum depth of the individual regression estimators, the  
356 minimum number of samples required to split an internal node, the minimum  
357 number of samples required to be at a leaf node, and others.

358 The gradient boosting algorithms have been implemented in several frame-  
359 works: GBR [93], XGBoost [94], LightGBM [95], and CatBoost [96]. XGBoost,  
360 LightGBM, and CatBoost are improved implementations of GBR. XGBoost was  
361 optimized for more accurate and faster predictions via regularization, custom  
362 loss functions, parallel processing, and other algorithm improvements. Light-  
363 GBM offers improved training speed, higher efficiency, better accuracy, lower  
364 memory use, and the ability to process large datasets by applying the Gradient-  
365 based One-Side Sampling (GOSS) method and parallel learning. CatBoost can

366 process categorical features to improve accuracy for datasets with categorical  
367 features, ordered boosting to fight overfitting, missing value support, and others.

#### 368 4. Implementation and results

369 The ML algorithms were implemented in the following Python-based open-  
370 source libraries: *scikit-learn* (DT, RF, KNN, and GBR) [93], *XGBoost* [94],  
371 *LightGBM* [95], and *CatBoost* [96]. The models were optimized, validated, and  
372 tested using the ten-fold cross-validation method. The  $w_{cr}$  and  $w_{max}$  datasets  
373 were randomly divided into training and test sets in the 80/20 proportion. The  
374 training set of each dataset was partitioned into ten groups. The models were  
375 trained on nine groups of the training set and validated on the remaining group.  
376 The process was repeated for the remaining groups of the training set until each  
377 group had served as the validation set. The final performance of the models was  
378 evaluated on the test data unseen by the models in training. Compared with the  
379 hold-out method, where the dataset is divided into training, validation, and test  
380 sets, with each set used for its purpose only, the ten-fold cross-validation method  
381 makes more samples available for model training and excludes model dependence  
382 on a particular random choice of the samples selected for the training, validation,  
383 and test sets. As a result, the ten-fold cross-validation method usually produces  
384 more accurate models with better generalization performance.

Figs. 2 and 3 demonstrate that the numerical ranges of the features ranged widely in the datasets, which is not ideal for ML models, as it might cause difficulties for the algorithms in finding optimal model parameters. Each feature value in the training set was standardized using Eq. (13) to make the features' scales uniform. Each feature in the test set was also standardized using the mean and standard deviation values of the feature obtained for the training set.

$$x' = \frac{x - \mu}{\sigma} \tag{13}$$

385 where  $x'$  is the standardized value of the input parameter,  $x$  is the original  
386 (non-standardized) value of the input parameter,  $\mu$  is the mean of the original  
387 values of the input parameter, and  $\sigma$  is the standard deviation of the original  
388 values of the input parameter.

Performance of the ML learning models was evaluated based on the mean squared error (MSE) values obtained for the test set calculated as follows.

$$MSE = \frac{1}{n} \sum_{i=1}^n (y - \hat{y})^2 \quad (14)$$

389 where  $n$  is the number of samples,  $y$  is the output value, and  $\hat{y}$  is the predicted  
390 output value.

Mean absolute error (MAE), mean absolute percentage error (MAPE), the coefficient of determination ( $R^2$ ), the minimum, maximum, mean, and coefficient of variation values of the prediction-to-FEA ratios, which are metrics commonly used for performance evaluation of ML models [97], calculated using the following equations were also determined for the training and test sets.

$$MAE = \frac{1}{n} \sum_{i=1}^n |y - \hat{y}| \quad (15)$$

$$MAPE = \frac{100}{n} \sum_{i=1}^n \left| \frac{y - \hat{y}}{y} \right| \quad (16)$$

$$R^2 = 1 - \frac{\sum_{i=1}^n (y - \hat{y})^2}{\sum_{i=1}^n (y - \bar{y})^2} \quad (17)$$

391 where  $\bar{y}$  is the mean of the  $y$  values.

392 Extensive hyperparameter tuning was carried out for each ML model using  
393 the grid and random searches to find optimal hyperparameter values that  
394 give the best model performance. The obtained optimal hyperparameters for

395 each ML model are listed below. The hyperparameter designations used in the  
396 Python libraries [93–96] are shown in parentheses. The hyperparameters not  
397 presented below had default values.

398 • DT:

- 399 – the maximum depth of the tree (`max_depth`): None for  $w_{cr}$  and  $w_{max}$ ,
- 400 – the minimum number of samples required to split an internal node  
401 (`min_samples_split`): 4 for  $w_{cr}$  and 2 for  $w_{max}$ ,
- 402 – the minimum number of samples at a leaf node (`min_samples_leaf`):  
403 2 for  $w_{cr}$  and  $w_{max}$ .

404 • RF:

- 405 – the number of trees in the forest (`n_estimators`): 80 for  $w_{cr}$  and 200  
406 for  $w_{max}$ ,
- 407 – the maximum depth of the tree (`max_depth`): None for  $w_{cr}$  and  $w_{max}$ ,
- 408 – the minimum number of samples required to split an internal node  
409 (`min_samples_split`): 2 for  $w_{cr}$  and  $w_{max}$ ,
- 410 – the minimum number of samples at a leaf node (`min_samples_leaf`):  
411 1 for  $w_{cr}$  and  $w_{max}$ .

412 • KNN

- 413 – the number of neighbors (`n_neighbors`): 5 for  $w_{cr}$  and 4 for  $w_{max}$ ,
- 414 – weight function (`weights`): uniform for  $w_{cr}$  and  $w_{max}$ ,
- 415 – the power parameter for the Minkowski metric (`p`): 1 for  $w_{cr}$  and  
416  $w_{max}$ ,
- 417 – leaf size (`leaf_size`): 20 for  $w_{cr}$  and 30 for  $w_{max}$ .

418 • GBR:

- 419 – learning rate (`learning_rate`): 0.1 for  $w_{cr}$  and  $w_{max}$ ,
- 420 – the number of boosting stages (`n_estimators`): 200 for  $w_{cr}$  and 1300
- 421 for  $w_{max}$ ,
- 422 – maximum depth of individual regression estimators (`max_depth`): 5
- 423 for  $w_{cr}$  and 9 for  $w_{max}$ ,
- 424 – the minimum number of samples required to split an internal node
- 425 (`min_samples_split`): 2 for  $w_{cr}$  and  $w_{max}$ ,
- 426 – the minimum number of samples at a leaf node (`min_samples_leaf`):
- 427 3 for  $w_{cr}$  and 4 for  $w_{max}$ .
  
- 428 • XGBoost:
  - 429 – learning rate (`eta`): 0.2 for  $w_{cr}$  and  $w_{max}$ ,
  - 430 – minimum loss reduction required to make a further partition on a
  - 431 leaf node of the tree (`gamma`): 1 for  $w_{cr}$  and  $w_{max}$ ,
  - 432 – the maximum tree depth of base learners (`max_depth`): 5 for  $w_{cr}$  and
  - 433 12 for  $w_{max}$ ,
  - 434 – the minimum sum of instance weight (hessian) needed in a child
  - 435 (`min_child_weight`): 3 for  $w_{cr}$  and 6 for  $w_{max}$ .
  
- 436 • LightGBM:
  - 437 – learning rate (`learning_rate`): 0.1 for  $w_{cr}$  and  $w_{max}$ ,
  - 438 – the number of boosting iterations (`num_iterations`): 100 for  $w_{cr}$  and
  - 439 3800 for  $w_{max}$ ,
  - 440 – maximum tree leaves for base learners (`num_leaves`): 50 for  $w_{cr}$  and
  - 441  $w_{max}$ ,
  - 442 – the minimum number of observations that must fall into a tree node
  - 443 for it to be added (`min_data_in_leaf`): 10 for  $w_{cr}$  and  $w_{max}$ ,

- 444 – maximum tree depth for base learners (`max_depth`): -1 (None) for
- 445  $w_{cr}$  and  $w_{max}$ ,
- 446 – the maximum number of bins (`max_bin`): 100 for  $w_{cr}$  and  $w_{max}$ .
- 447 • CatBoost
- 448 – learning rate (`learning_rate`): 0.03 for  $w_{cr}$  and  $w_{max}$ ,
- 449 – the number of iterations (`iterations`): 850 for  $w_{cr}$  and 4000 for
- 450  $w_{max}$ ,
- 451 – tree depth (`depth`): 6 for  $w_{cr}$  and 11 for  $w_{max}$ ,
- 452 – L2 regularization term coefficient of the cost function (`l2_leaf_reg`):
- 453 3 for  $w_{cr}$  and 1 for  $w_{max}$ ,
- 454 – the amount of randomness to use for scoring splits when the tree
- 455 structure is selected (`random_strength`): 1 for  $w_{cr}$  and 2 for  $w_{max}$ .

456 Figs. 7 and 8 show the performance of the developed ML models with the op-  
 457 timal hyperparameters for predicting  $w_{cr}$  and  $w_{max}$ , respectively. The compar-  
 458 isons of the ML model predictions with FE simulation results are demonstrated  
 459 for the training and test datasets in each figure. The values of  $R^2$ , minimum,  
 460 maximum, mean, and coefficient of variation of the prediction-to-FEA ratios  
 461 are presented in Figs. 7 and 8. The MSE, MAE, and MAPE values are given in  
 462 Tables 1 and 2.

Table 1: Performance metrics of ML models for predicting elastic buckling loads of steel cellular beams,  $w_{cr}$  (Train/Test)

Model	MSE ((kN/m) <sup>2</sup> )	MAE (kN/m)	MAPE (%)
DT	155.94/1538.26	6.04/19.07	2.35/7.05
RF	83.79/682.24	4.44/13.00	1.83/5.27
KNN	1320.87/2617.14	21.09/28.99	10.22/12.66
GBR	39.68/319.27	3.85/7.66	1.99/3.24
XGBoost	48.44/294.91	4.51/8.59	2.51/3.95
LightGBM	41.88/366.81	3.57/7.56	1.82/3.06
CatBoost	33.90/295.43	3.16/6.15	1.52/2.48

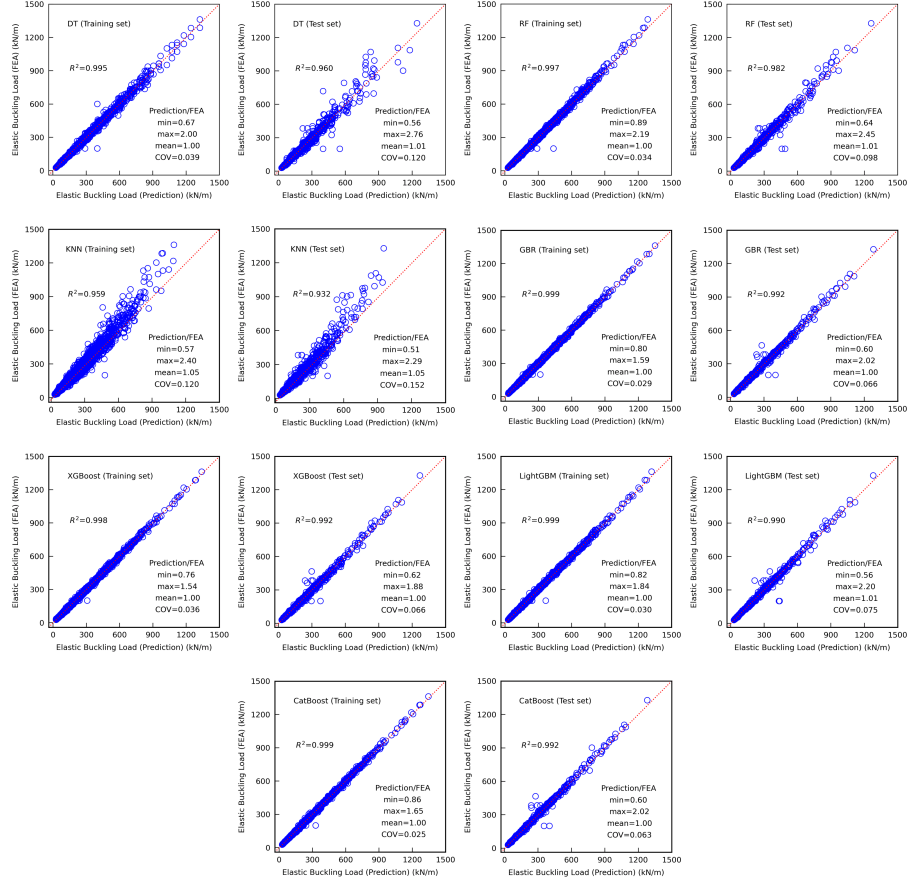


Figure 7: Performance of ML models for predicting elastic buckling load of steel cellular beams

Table 2: Performance metrics of ML models for predicting ultimate loads of steel cellular beams,  $w_{max}$  (Train/Test)

Model	MSE ((kN/m) <sup>2</sup> )	MAE (kN/m)	MAPE (%)
DT	15.99/20.25	2.08/2.37	1.90/2.18
RF	16.01/20.17	2.08/2.38	1.90/2.18
KNN	18.43/22.61	2.18/2.49	1.99/2.27
GBR	16.01/20.24	2.08/2.38	1.90/2.18
XGBoost	16.03/20.13	2.09/2.39	1.92/2.19
LightGBM	16.10/20.10	2.11/2.40	1.94/2.20
CatBoost	16.05/20.17	2.10/2.39	1.92/2.19

463 As can be seen from Fig. 7 and Table 1, CatBoost, XGBoost, and GBR  
 464 demonstrated comparable performances in predicting  $w_{cr}$  for the test set. The

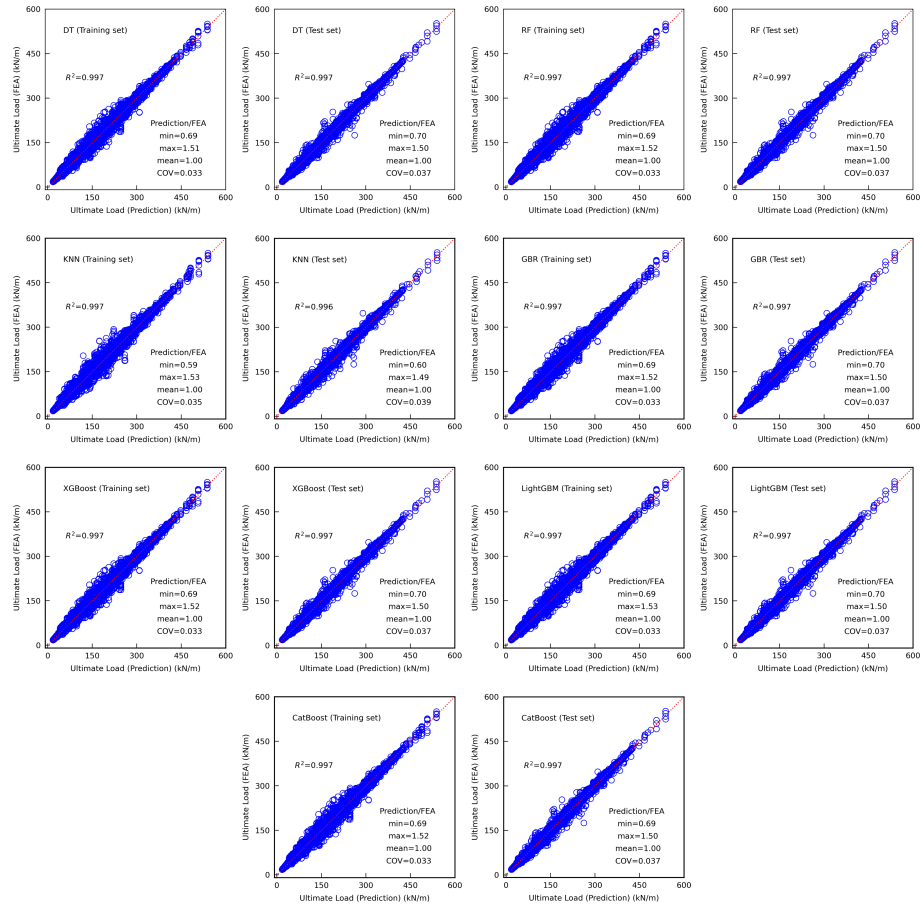


Figure 8: Performance of ML models for predicting ultimate load of steel cellular beams

465 performance metrics for LightGBM were slightly worse than those for CatBoost,  
 466 XGBoost, and GBR. KNN provided inferior performance compared with other  
 467 considered ML models. Fig. 8 and Table 2 show that all models performed  
 468 well in predicting  $w_{max}$ , with KNN providing slightly worse metrics than other  
 469 algorithms. It is worth reminding that the ultimate load dataset included 78390  
 470 samples and was significantly larger than the elastic buckling load dataset with  
 471 3645 samples. The good predictions of the ultimate load by all considered  
 472 ML models, which was not the case for the elastic buckling dataset, highlight

473 that good data with a very large number of samples contributes more to the  
474 accuracy of ML models than the ML algorithm differences. It can also be seen  
475 from comparisons of the performance metrics for the training and test sets that  
476 the created ML models with the optimal hyperparameters have a reasonably  
477 good generalization performance.

478 Developed ML models can be accessed at the following link: [https://ww](https://www.kaggle.com/vitdegyarev/cellular-beams-ml-models)  
479 [w.kaggle.com/vitdegyarev/cellular-beams-ml-models](https://www.kaggle.com/vitdegyarev/cellular-beams-ml-models). An interactive  
480 notebook for predicting the elastic buckling and ultimate loads of steel cellular  
481 beams with the developed ML models can be found at the following link: [https:](https://www.kaggle.com/vitdegyarev/ml-models-for-cellular-beams?scriptVersionId=63075739)  
482 [//www.kaggle.com/vitdegyarev/ml-models-for-cellular-beams?scrip](https://www.kaggle.com/vitdegyarev/ml-models-for-cellular-beams?scriptVersionId=63075739)  
483 [tVersionId=63075739](https://www.kaggle.com/vitdegyarev/ml-models-for-cellular-beams?scriptVersionId=63075739).

## 484 **5. Relative feature importance and feature dependence**

485 Structural engineers often perceive ML methods as black boxes because hu-  
486 mans cannot easily explain and interpret ML predictions. To remove this barrier  
487 to adopting ML methods, several ML explainability and interpretability tech-  
488 niques are available, including relative feature importance, partial dependence,  
489 feature interactions, and SHAP [98]. These techniques shed light on why and  
490 how an ML model made its predictions and expose how ML model predictions  
491 compare with mechanics-based knowledge. The application of the explainability  
492 and interpretability methods to the developed ML models is described in this  
493 section.

494 Relative effects of the features on the  $w_{cr}$  and  $w_{max}$  predictions by each con-  
495 sidered ML model were analyzed using the permutation and SHAP methods.  
496 The permutation feature importance is a decrease in a model score when the  
497 feature values are randomly shuffled (permuted). A feature with a more sig-  
498 nificant score decrease is more important than others. The model score in the

499 form of coefficient of determination,  $R^2$ , was used in this study. The random  
500 shuffling of values is repeated several times for each feature to obtain the mean  
501 and the standard deviation of the permutation importance score.

502 The SHAP method [86] aims to explain a prediction for a sample by deter-  
503 mining the contribution of each feature to the prediction by computing Shapley  
504 values from coalitional game theory [99]. The Shapley value represents the av-  
505 erage contribution of one player, which is a model feature in our case, to the  
506 model predictions taken for all possible combinations, which may consist of all  
507 dataset samples or a predefined portion of them. SHAP uses an additive feature  
508 attribution method – a linear explanation model of the summation of present  
509 features. The feature importance is determined based on the absolute average  
510 Shapley values. Features with larger Shapley values are more important than  
511 others. SHAP feature importance is based on the magnitude of feature attri-  
512 butions, while permutation feature importance is based on the decrease in the  
513 model performance. Thus, the relative feature importance predicted by these  
514 two methods might be different.

515 The relative feature importance was determined for all considered ML models  
516 using both methods. The relative feature importance plots were similar for all  
517 models. Therefore, the relative feature importance for the CatBoost models,  
518 which are ones of the most accurate models for predicting  $w_{cr}$  and  $w_{max}$ , is  
519 presented and discussed hereafter. Fig. 9 shows permutation and SHAP feature  
520 importance plots for the optimized CatBoost models for predicting  $w_{cr}$  and  
521  $w_{max}$ .

522 The relative feature importance in predicting the elastic buckling load,  $w_{cr}$ ,  
523 of steel cellular beams is discussed first. The span length,  $L$ , has the most  
524 significant importance according to both methods, which was expected. The  
525 next important beam parameters are the flange width,  $b_f$ , the web thickness,

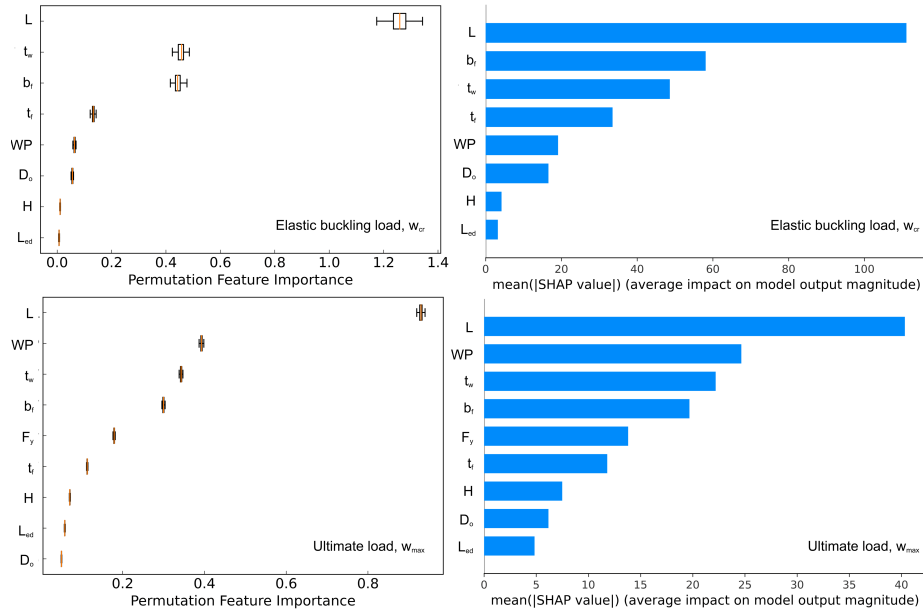


Figure 9: Permutation and SHAP feature importance for CatBoost models

526  $t_w$ , and the flange thickness,  $t_f$ . The permutation method indicated that  $t_w$   
 527 is more important than  $b_f$  in predicting  $w_{cr}$ , while the SHAP method showed  
 528  $b_f$  above  $t_w$ . However, the difference in the importance scores for  $b_f$  and  $t_w$  is  
 529 small, especially per the permutation method. These results compare well with  
 530 the conclusions made in [29], indicating that the CatBoost model can capture  
 531 the mechanics of the cellular beam behavior. The relative importance of the  
 532 web post width,  $WP$ , the opening diameter,  $D_o$ , the beam height,  $H$ , and the  
 533 opening end distance,  $L_{ed}$ , have relatively small importance in predicting  $w_{cr}$   
 534 according to both methods.

535 The permutation and SHAP relative feature importance plots for  $w_{max}$   
 536 demonstrate that the span length,  $L$ , is the most important feature, followed  
 537 by  $WP$ ,  $t_w$ ,  $b_f$ ,  $F_y$ , and  $t_f$ . It should be noted that  $WP$  has a more significant  
 538 impact on  $w_{max}$  than on  $w_{cr}$ . These results align with the conclusion made  
 539 in [29] and confirm the positive contribution of the web post plastic behavior

540 to the strength of steel cellular beams mentioned in Section 2. The relative  
 541 importance of  $H$ ,  $D_o$ , and  $L_{ed}$  for predicting  $w_{max}$  is minor.

542 SHAP feature importance plots provide useful information, which is, how-  
 543 ever, somewhat limited. SHAP summary plots shown in Fig. 10 are more  
 544 informative as they combine feature importance and feature effects. Each point  
 545 on the summary plots represents a Shapley value for a dataset sample. The  
 546 color shows the feature value from low (blue) to high (red). Points with the  
 547 same Shapley values are scattered vertically to demonstrate their distribution  
 548 for each feature. The order of the features follows their importance; so, it is  
 549 the same as shown in Fig. 9. The SHAP summary plots presented in Fig.  
 550 10 indicate that  $w_{cr}$  and  $w_{max}$  increase when the beam span reduces and vice  
 551 versa. Wide web posts have higher  $w_{cr}$  and  $w_{max}$ , which decrease when the  
 552 web post width reduces. Greater values of  $t_w$ ,  $b_f$ ,  $t_f$ , and  $L_{ed}$  produce higher  
 553  $w_{cr}$  and  $w_{max}$ , whereas an increase in the opening diameter  $D_o$  results in  $w_{cr}$   
 554 and  $w_{max}$  reductions. The beam height  $H$  affects  $w_{cr}$  and  $w_{max}$  differently:  
 555  $w_{cr}$  goes down when  $H$  increases, while  $w_{max}$  increases when  $H$  goes up. The  
 556 reduction of  $w_{cr}$  with an increase in  $H$  can be explained by an increase in the  
 557 web post slenderness, which results in the elastic buckling load reduction.

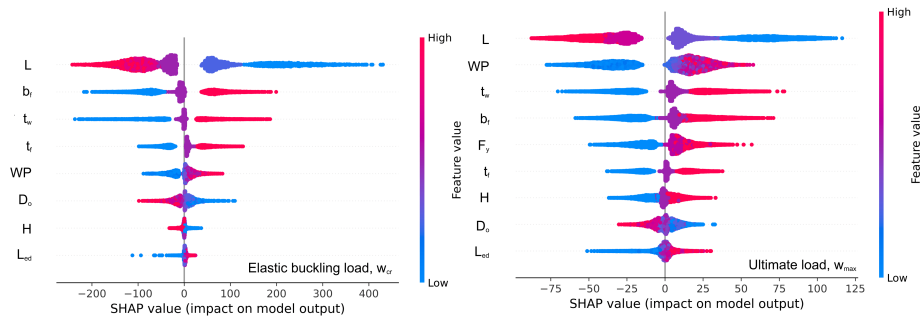


Figure 10: SHAP summary plots for CatBoost models

558 SHAP dependence plots given in Figs. 11 and 12 for  $w_{cr}$  and  $w_{max}$  illus-  
 559 trate exact relationships between feature values and predictions. Each point

560 represents a prediction for a dataset sample. Feature values are shown on the  
 561 horizontal axes, while SHAP values are given on the vertical axes. The SHAP  
 562 values demonstrate the magnitude of change in  $w_{cr}$  and  $w_{max}$  when the feature's  
 563 value is known. The color of each point corresponds to the second feature, which  
 564 was determined by the algorithm to have the highest interaction with the con-  
 565 sidered feature shown on the horizontal axis.

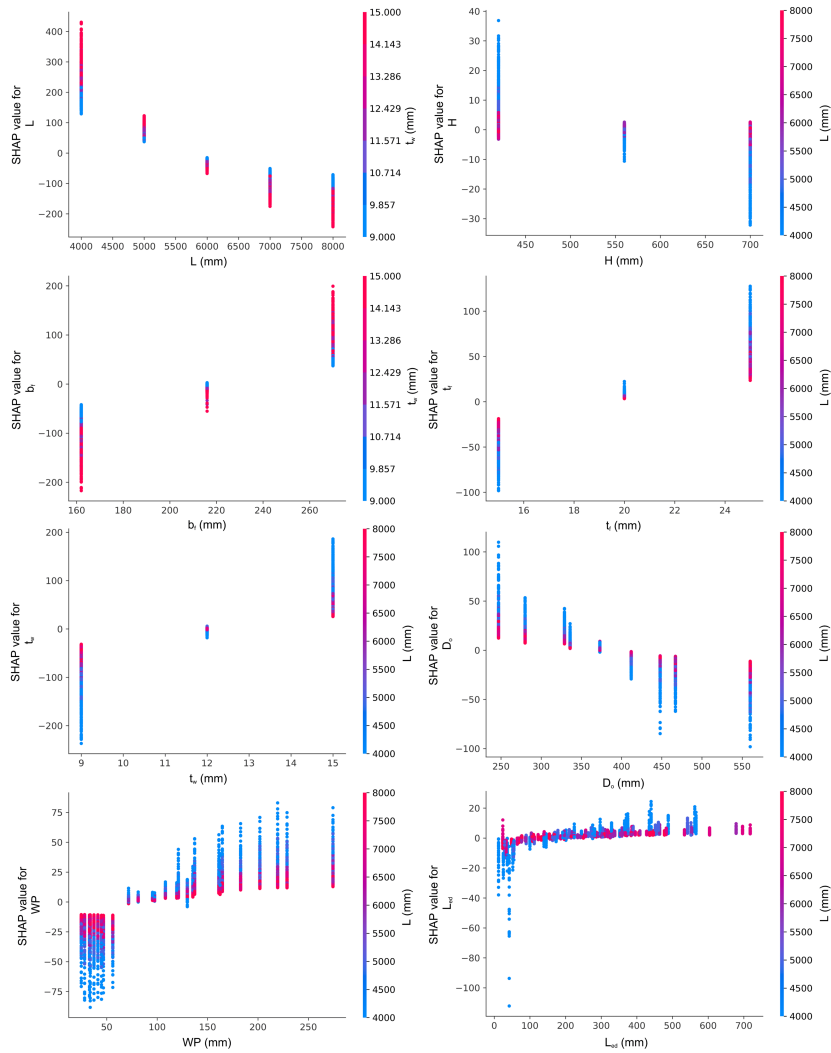


Figure 11: SHAP dependence plots for CatBoost model for predicting elastic buckling load

566 The SHAP dependence plots for  $w_{cr}$  show that  $L$  and  $b_f$  have the highest  
 567 interactions with  $t_w$ , while other features interact with  $L$  most frequently. An  
 568 increase in  $L$  results in an exponential decrease in  $w_{cr}$ , which is more pronounced  
 569 for the cellular beams with thicker webs. An increase in  $H$  results in reductions  
 570 of  $w_{cr}$  for the beams with short spans and smaller reductions or no reduction  
 571 for the beams with long spans, which can be seen from the comparison of the  
 572 SHAP values for the beams with long spans (red dots) with the SHAP values for  
 573 the beams with short spans (blue dots). These results indicate that the elastic  
 574 buckling load of the beams with short spans was likely governed by the local web  
 575 buckling. In contrast, the elastic buckling load of the beams with long spans was  
 576 likely governed by the global lateral-torsional buckling of the beams, which was  
 577 less sensitive to the changes in  $H$  for the beams considered in this study. The  
 578 elastic buckling loads increase when  $b_f$  increases, especially for the beams with  
 579 thicker webs. The elastic buckling load,  $w_{cr}$ , increases when  $t_f$  and  $t_w$  increase,  
 580 especially in the beams with short spans. The elastic buckling loads reduce  
 581 when  $D_o$  goes up. The  $w_{cr}$  reduction is more significant due to the  $D_o$  increase  
 582 for the cellular beams with short spans. When  $WP$  increases,  $w_{cr}$  increases,  
 583 especially for the beams with short spans. The plot also shows that web posts  
 584 with widths of 56 mm and narrower contribute to  $w_{cr}$  reductions, indicated by  
 585 the negative SHAP values, while web posts of 72 mm wide and wider contribute  
 586 to  $w_{cr}$  positively. An increase in  $L_{ed}$  results in a more significant increase in  $w_{cr}$   
 587 for the beams with short spans and a smaller increase in  $w_{cr}$  for those with long  
 588 spans. It should be noted that the beam elastic buckling loads in the dataset  
 589 were obtained for different buckling modes, including global lateral-torsional  
 590 buckling of the beams, local buckling of the web posts, and their interaction.  
 591 Therefore, the effects of the ML model features discussed above reflect possible  
 592 changes in the buckling modes when the beam geometry changes.

593 The SHAP dependence plots for  $w_{max}$  demonstrate that the strongest in-  
 594 teractions are between  $L$  and  $t_w$ ,  $H$  and  $D_o$ ,  $b_f/t_f$  and  $WP$ , and  $L_{ed}$  and  $b_f$ .  
 595 All other features of the ultimate load model interact with  $L$  the most. An  
 596 increase in  $L$  results in a  $w_{max}$  reduction, which is more pronounced in the cel-  
 597 lular beams with thicker webs. Increases in  $H$ ,  $b_f$ ,  $t_f$ , and  $t_w$  cause an increase  
 598 in  $w_{max}$ , which goes down when  $D_o$  increases. An increase in  $WP$  makes the  
 599 beam ultimate load higher, which is more pronounced for the beams with short  
 600 spans. Similar to the observed effect of  $WP$  on  $w_{cr}$ , web post widths up to 56  
 601 mm have a negative contribution to the beam ultimate load, while web posts  
 602 of 72 mm wide and wider contribute to the beam ultimate load positively. It  
 603 implies that the beam ultimate load in the dataset was governed by the web  
 604 post strength when  $WP$  was 56 mm or lower. The beam ultimate load becomes  
 605 higher when  $L_{ed}$  and  $F_y$  increase. The positive effect of  $F_y$  on  $w_{max}$  is more  
 606 significant in the beams with short spans and when  $F_y$  increases from 235 to  
 607 355 MPa compared with the  $F_y$  increase from 355 to 440 MPa.

608 Fig. 13 shows contour plots of  $w_{cr}$  predicted by the developed CatBoost  
 609 model as functions of  $H/D_o$  and  $S_o/D_o$  (where  $S_o$  is the center-to-center spacing  
 610 of the web openings) for the beams with different span lengths and cross-section  
 611 dimensions. The beam designations are presented in the  $L-H-t_w-b_f-t_f$  format,  
 612 with all dimensions in mm. Fig. 13 demonstrates that  $S_o/D_o$  has a greater  
 613 influence on  $w_{cr}$  than  $H/D_o$  for the beams with short spans. For many short-  
 614 span beams, an increase in  $S_o/D_o$  from 1.1 to 1.3 results in a greater increase  
 615 in  $w_{cr}$  than a further increase in  $S_o/D_o$  from 1.3 to 1.49. It indicates that  
 616 web opening spacing of approximately  $1.3D_o$  is optimal for many short-span  
 617 beams. Only short-span beams with  $H=420$  mm and  $t_w=9$  mm demonstrate  
 618 an approximately uniform  $w_{cr}$  increase when  $S_o/D_o$  increases from 1.1 to 1.49.  
 619 The long-span beams show a wider variety of the  $w_{cr}$  contour shapes. For

620 example,  $H/D_o$  has a more significant effect on  $w_{cr}$  than  $S_o/D_o$  for the beam  
621 with  $H=420$  mm,  $t_w=9$  mm,  $b_f=162$  mm, and  $t_f=15$  mm compared with other  
622 analyzed beams. The  $w_{cr}$  values for the 8000-420-9-162-15 and 8000-700-15-  
623 162-15 beams reduce slightly when  $S_o/D_o$  increase from 1.1 to 1.3 and increase  
624 with the further increase in  $S_o/D_o$  from 1.3 to 1.49. However, it should be noted  
625 that the absolute magnitude of the  $w_{cr}$  change is relatively small in those cases.  
626 The contour plots also show the effects of the cross-section dimensions on the  
627  $w_{cr}$  values of the cellular beams discussed earlier in the paper.

628 Figs. 14 and 15 present contour plots of  $w_{max}$  predicted by the CatBoost  
629 model as functions of  $H/D_o$  and  $S_o/D_o$  for the cellular beams made from steel  
630 with  $F_y$  of 235 and 440 MPa, respectively. The beam designation format is as  
631 described previously, with the steel yield strength added at the end. Similar  
632 to  $w_{cr}$ ,  $S_o/D_o$  shows a more significant effect on  $w_{max}$  than  $H/D_o$  for most of  
633 the considered beams. The effect of the opening diameter on  $w_{max}$  is more pro-  
634 nounced in the  $H/D_o$  range from 1.25 to approximately 1.45 for many beams.  
635 A further increase in  $H/D_o$  at a constant  $S_o/D_o$  value changes  $w_{max}$  insignif-  
636 icantly. It can also be seen from the contour plots that for some beams (see  
637 4000-420-15-162-15-235, 7000-420-15-162-15-235, 4000-420-15-270-15-440, and  
638 7000-700-9-270-15-440, for example), the effects of  $H/D_o$  varying in the range  
639 from 1.25 to 1.45 on  $w_{max}$  are relatively small when  $S_o/D_o$  is low. They be-  
640 come more pronounced as  $S_o/D_o$  increases. The  $S_o/D_o$  of approximately 1.3 is  
641 optimal for many considered beams. The effects of the cross-section dimensions  
642 on  $w_{max}$  discussed earlier in the paper can also be seen from Figs. 14 and 15.

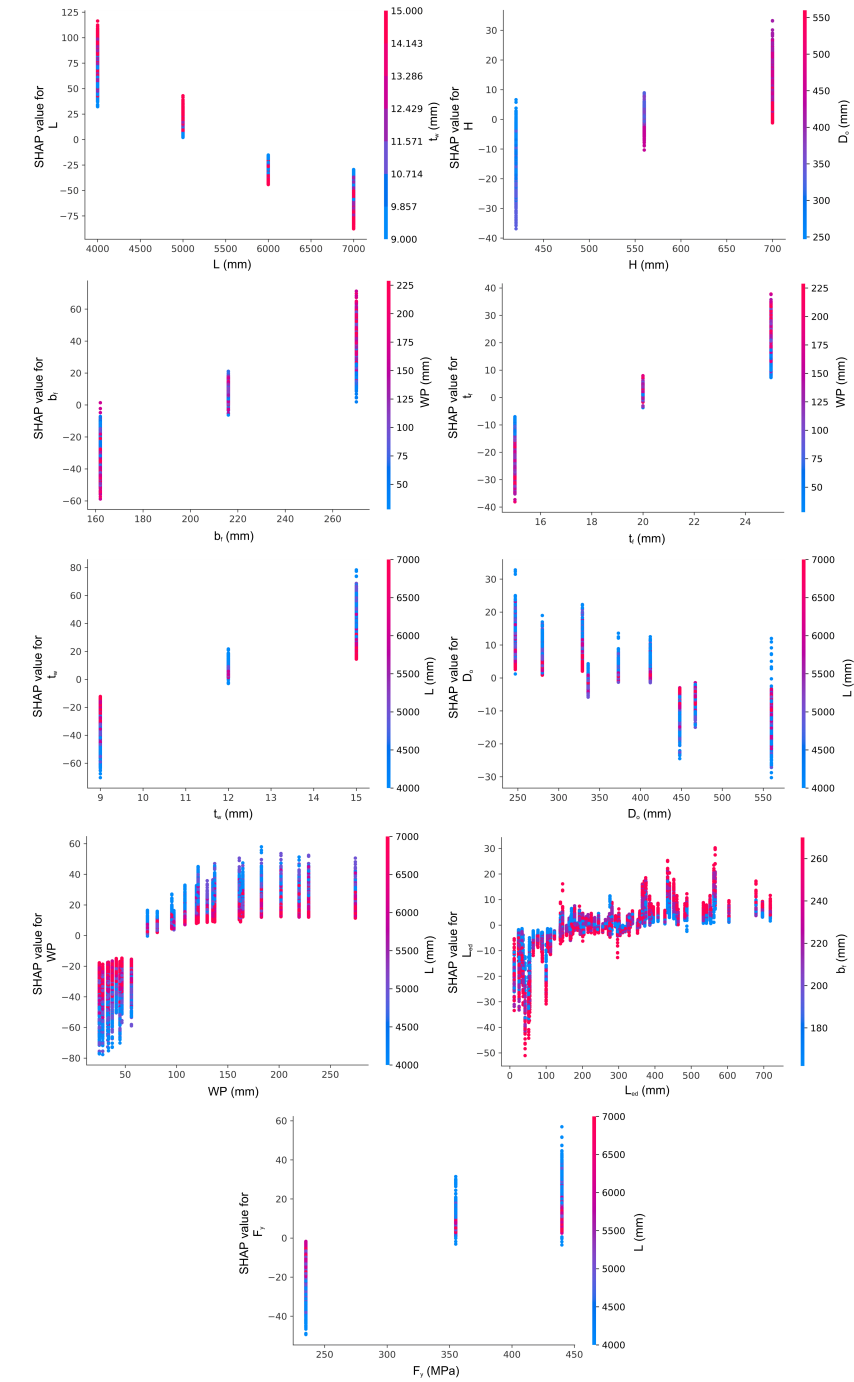


Figure 12: SHAP dependence plots for CatBoost model for predicting ultimate load

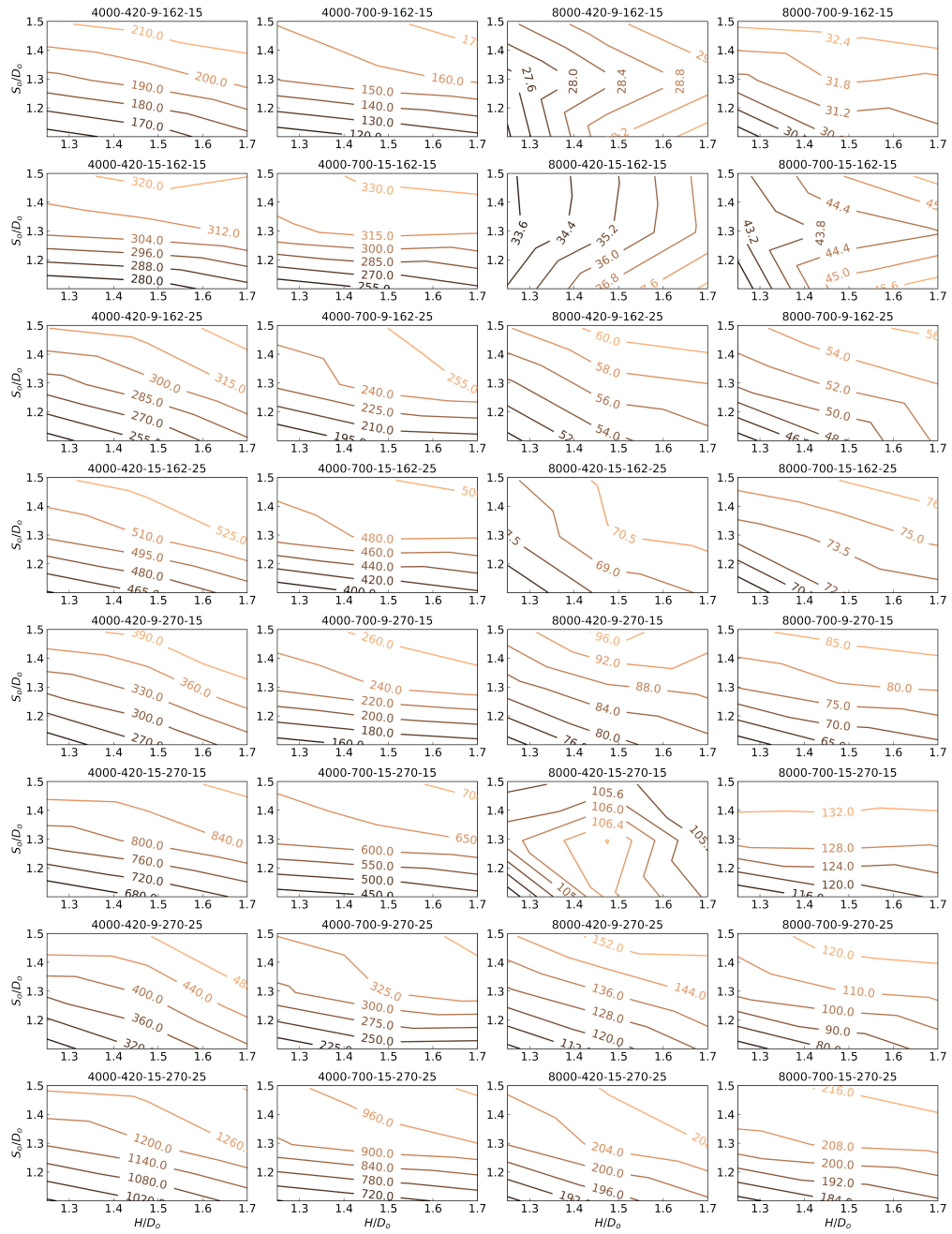


Figure 13: Contour plots of  $w_{cr}$  (kN/m) as functions of  $H/D_o$  and  $S_o/D_o$

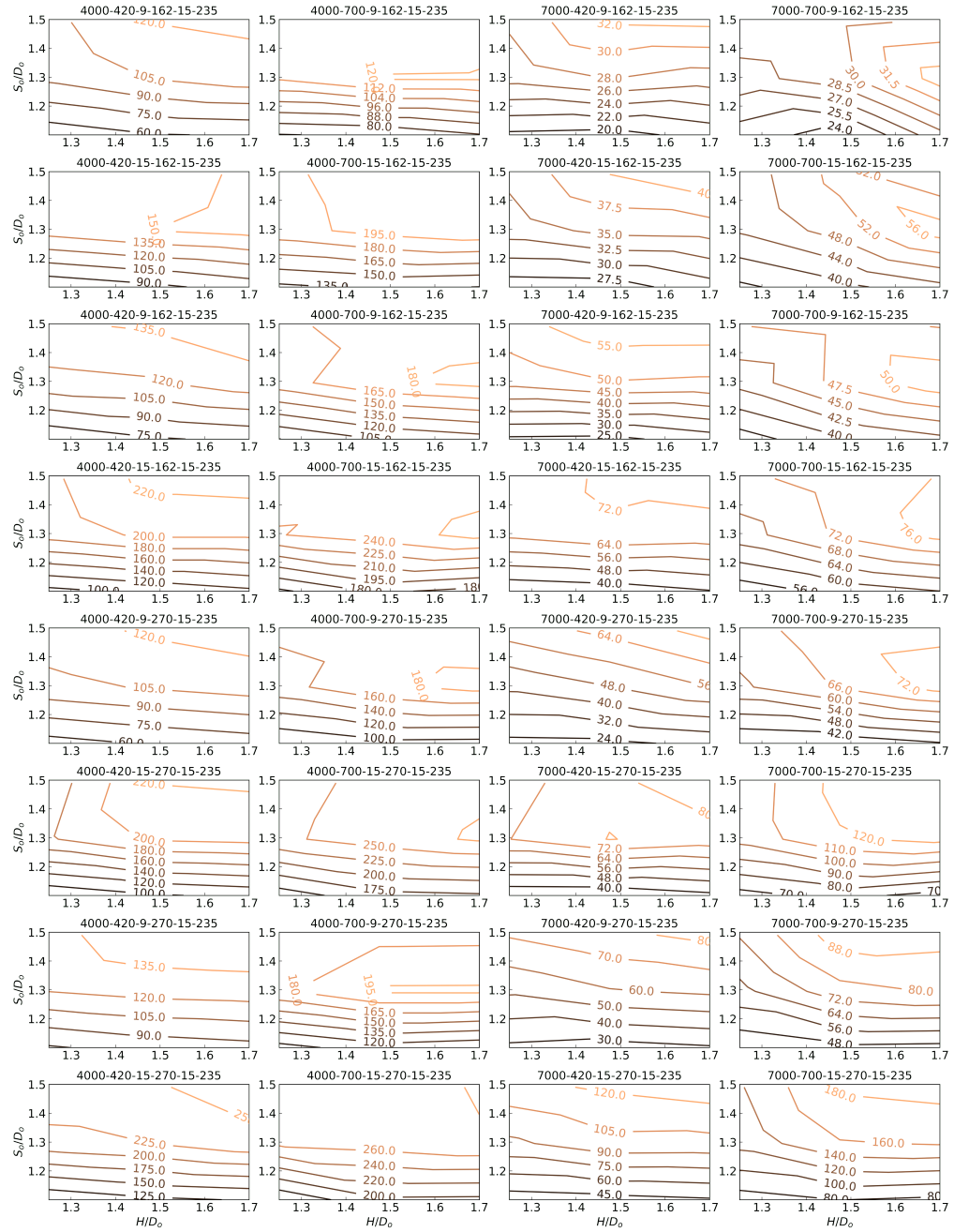


Figure 14: Contour plots of  $w_{max}$  (kN/m) as functions of  $H/D_o$  and  $S_o/D_o$  for beams made from 235 MPa steel

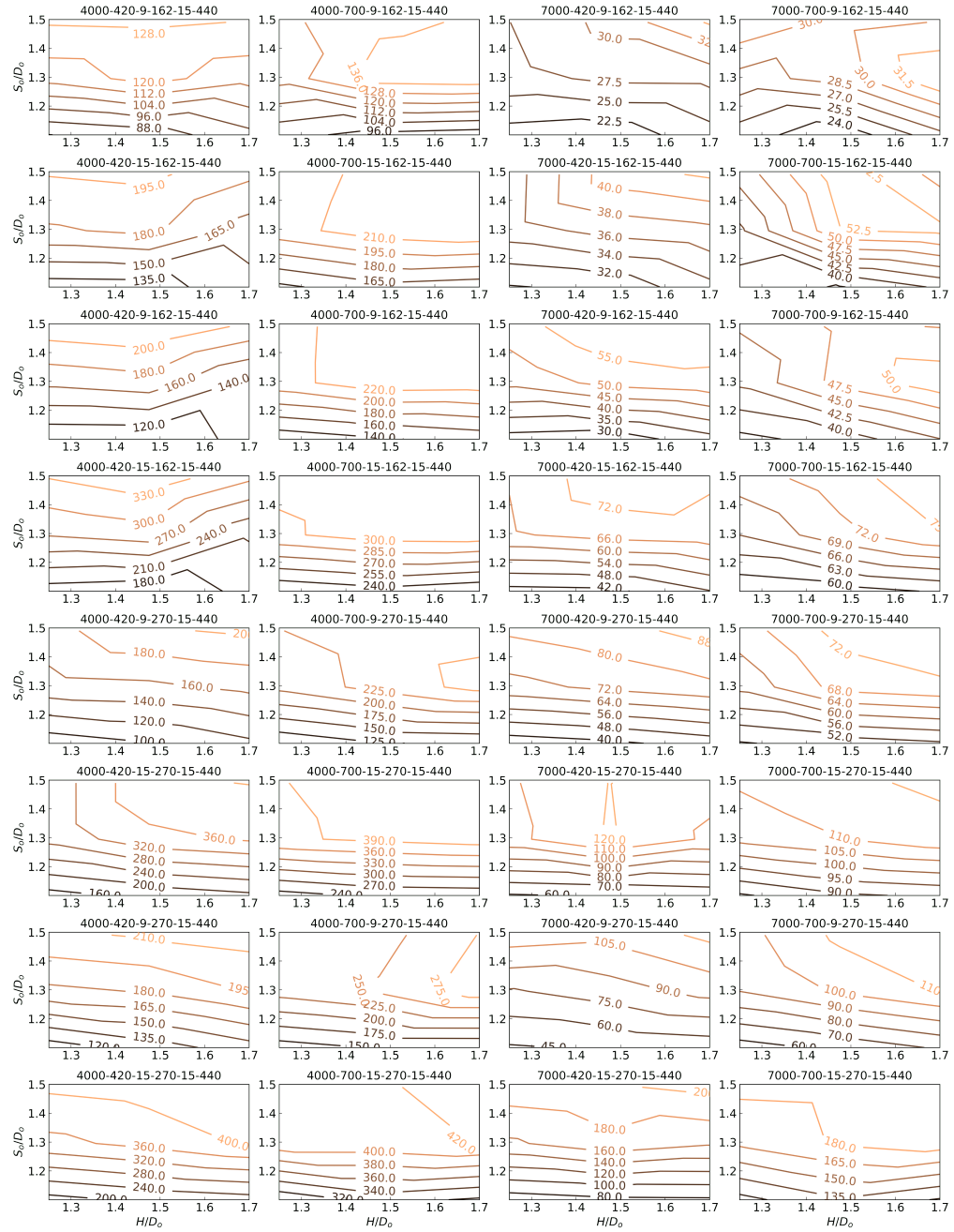


Figure 15: Contour plots of  $w_{max}$  (kN/m) as functions of  $H/D_o$  and  $S_o/D_o$  for beams made from 440 MPa steel

643 **6. Comparisons of ultimate loads of cellular beams predicted by ML**  
644 **models, SCI P355, and AISC Design Guide 31**

645 The ultimate loads of cellular beams predicted by the developed ML models  
646 were compared with the nominal beam strengths determined per SCI P355 [2]  
647 and AISC Design Guide 31 [87]. According to SCI P355 and AISC Design  
648 Guide 31, the cellular beam strength may be governed by shear resistance of  
649 perforated beam section, shear resistance of solid beam section, shear buckling  
650 resistance of perforated web, bending resistance of beam at the centerline of  
651 opening, bending resistance of tees, web post shear resistance, and web post  
652 buckling resistance. The beam, tee, and web post resistances are computed  
653 per EN 1993-1-1 [12] and EN 1993-1-5 [100] in SCI P355 and per AISC 360  
654 [101] in AISC Design Guide 31. The most significant differences between the  
655 SCI P355 and AISC Design Guide 31 provisions are in the web post buckling  
656 resistance and lateral-torsional buckling calculations [102]. In SCI P355, the  
657 web post buckling resistance is calculated using analytical equations, which  
658 account for the web post slenderness, while AISC Design Guide 31 adopted  
659 empirical equations from SCI P100 [27]. SCI P355 also requires checking web  
660 shear buckling near openings, whereas AISC Design Guide 31 does not include  
661 such a requirement.

662 The SCI P355 provisions apply to cellular beams with the following geo-  
663 metric limits:  $H/D_o \geq 1.25$ ,  $2.0 \geq S_o/D_o \geq 1.3$ ,  $L_{ed}/D_o \geq 0.5$ , and the  
664 depth of tees not less than  $t_f+30$  mm. The beams considered in the study  
665 had the following parameters:  $1.70 \geq H/D_o \geq 1.25$ ,  $1.49 \geq S_o/D_o \geq 1.10$ ,  
666  $1.49 \geq L_{ed}/D_o \geq 0.04$ , and the depth of tees between  $t_f+29.5$  mm and  $t_f+136.5$   
667 mm.  $S_o/D_o$ ,  $L_{ed}/D_o$ , and the depth of tees of some beams did not comply  
668 with the SCI P355 limits. Therefore, the SCI P355 predictions were com-  
669 pared with the FE simulation results for all beams and 17,982 beams that met

670 the geometric limits. AISC Design Guide 31 applies to cellular beams with  
671  $1.75 \geq H/D_o \geq 1.25$  and  $1.50 \geq S_o/D_o \geq 1.08$ . All beams considered in the  
672 present study complied with the AISC Design Guide 31 limits.

673 Fig. 16 compares the ultimate loads of the cellular beams from the FE  
674 simulations with those predicted by the developed ML models, SCI P355, and  
675 AISC Design Guide 31. Fig. 16 clearly shows that the developed ML models  
676 predict the ultimate loads of the cellular beams considerably better than SCI  
677 P355 and AISC Design Guide 31. For the best models, the mean ratio and the  
678 coefficient of variation of the ML predictions to the FE simulation results are  
679 1.00 and 0.034, respectively. The coefficient of determination,  $R^2$ , is 0.997. The  
680 corresponding metrics for SCI P355 are 0.75, 0.253, and 0.638 for all beams  
681 and 0.75, 0.298, and 0.535 for the beams meeting the geometric limits. It is  
682 interesting to note that the SCI P355 provisions demonstrate better comparison  
683 with the FE simulation results when all beams are considered neglecting the  
684 geometric limits. AISC Design Guide 31 showed even worse accuracy than SCI  
685 P355, characterized by the mean ratio and the coefficient of variation of the  
686 prediction-to-FEA ratios of 0.69 and 0.429, and the coefficient of determination  
687 of 0.416.

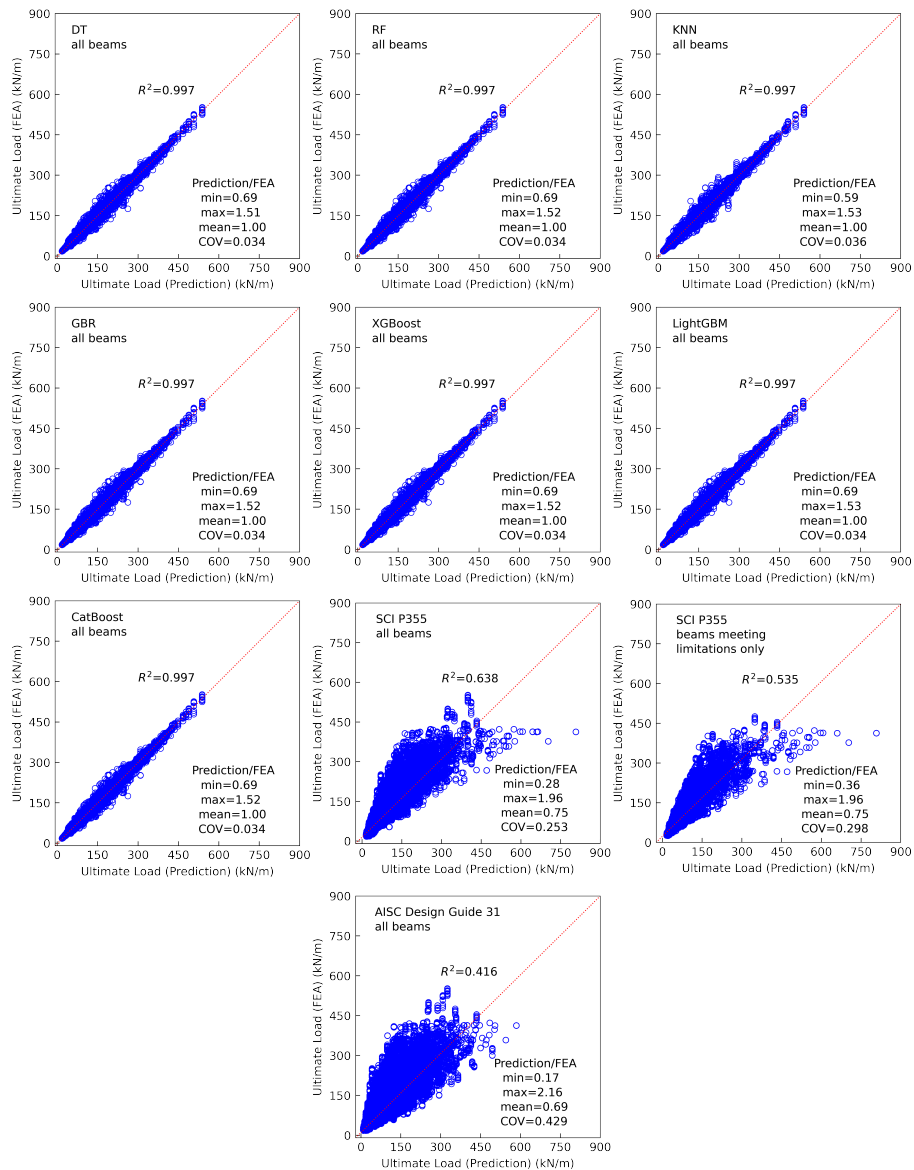


Figure 16: Comparisons of ultimate loads of steel cellular beams predicted by ML models, SCI P355, and AISC Design Guide 31 with FE simulation results

688 **7. Web application**

689 A user-friendly web application was created in the Streamlit framework (<https://streamlit.io>) to predict the elastic buckling and ultimate loads of  
 690 [tps://streamlit.io](https://streamlit.io)) to predict the elastic buckling and ultimate loads of

691 steel cellular beams with the ML models developed in the present work. Fig.  
692 17 demonstrates a flow chart of the web application.

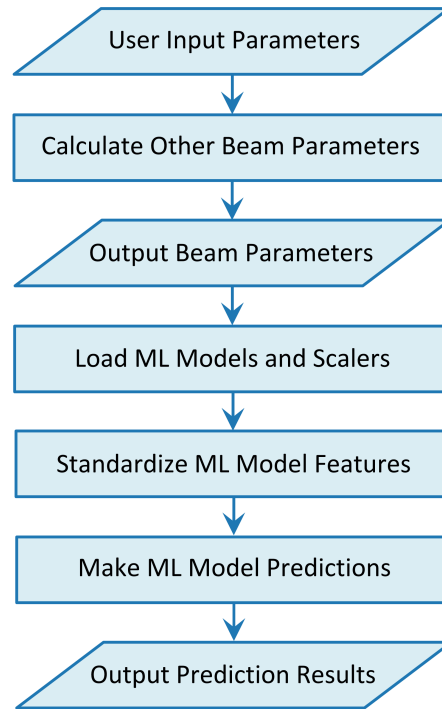


Figure 17: Flow chart of the web application

693 In the beginning, the user specifies the following parameters via the web  
694 application sliders and radio buttons:  $L$ ,  $H$ ,  $b_f$ ,  $t_f$ ,  $t_w$ ,  $H/D_o$ ,  $S_o/D_o$ , and  $F_y$ .  
695 Ranges of the parameters available in the application correspond to the feature  
696 ranges in the datasets used for the ML training. At the next step, the following  
697 parameters are computed:  $D_o$ ,  $S_o$ ,  $L_{ed}$ , the number of openings evenly spaced  
698 along the beam length, the cellular beam weight, and the percentage of the  
699 beam weight reduction due to the openings compared with the identical solid-  
700 web beam. The parameters specified by the user and the computed ones are  
701 displayed on the screen. Next, the developed ML models and scalers are loaded;  
702 the features are standardized, and predictions by all ML models considered

703 in this study are made and displayed. The code runs automatically after any  
 704 change of input variables. The prediction process takes only several seconds.  
 705 The graphical user interface of the web application is presented in Fig. 18.

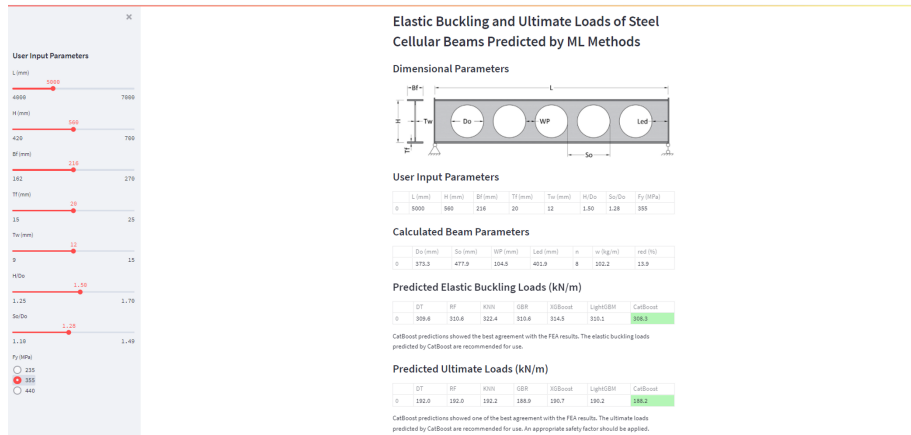


Figure 18: Graphical user interface of the developed web application

706 It was found challenging to deploy the web application with all consid-  
 707 ered ML to cloud platforms due to the application size and required compu-  
 708 tational resources, which exceeded the limits of free cloud accounts. There-  
 709 fore, a lite version of the application based on CatBoost predictions was cre-  
 710 ated and successfully deployed on Heroku at the following address: <https://scba-cb.herokuapp.com/>. The deployed lite version of the application  
 712 opens and runs in any web browser on any device, including mobile.

713 It should be noted that the computational resources provided by the free  
 714 Heroku account are sufficient for running the application by one user at a time.  
 715 Multiple users can open the application, but it crashes when two or more users  
 716 run the computations simultaneously. If that happens, it is recommended to  
 717 close the application and use it later. The use of a paid Heroku account, which  
 718 offers more powerful computational resources, would resolve this issue.

719 The source codes of the full and lite application versions can be accessed

720 on GitHub at <https://github.com/vitdegtyarev/SCBA-Streamlit> and  
721 <https://github.com/vitdegtyarev/SCBA-Streamlit-CB>, respectively. The  
722 GitHub pages include instructions on how the web applications can be used  
723 independently from the cloud services on a local machine.

## 724 **8. Conclusions**

725 ML models for predicting the elastic buckling and ultimate loads of steel  
726 cellular beams were developed and optimized using the following algorithms:  
727 decision tree (DT), random forest (RF), k-nearest neighbor (KNN), gradient  
728 boosting regressor (GBR), extreme gradient boosting (XGBoost), light gradient  
729 boosting machine (LightGBM), and gradient boosting with categorical features  
730 support (CatBoost). Large datasets of FE simulation results from the literature  
731 [29], validated against experimental data, were employed to train and evaluate  
732 the ML models implemented in open-source Python-based libraries.

733 The ML models were optimized by tuning their hyperparameters via ex-  
734 tensive grid and random searches and validated through the ten-fold cross-  
735 validation method. The final evaluation of the ML models was performed on  
736 the test sets unseen by the models during training. The elastic buckling and  
737 ultimate loads predicted by the optimized ML models demonstrated excellent  
738 agreements with the numerical data. The accuracy of the ultimate load predic-  
739 tions by the ML models exceeded the accuracy provided by the existing design  
740 provisions for steel cellular beams. An interactive Python-based notebook for  
741 predicting the elastic buckling and ultimate loads of steel cellular beams using  
742 the developed optimized ML models was created and made publicly available  
743 at the following link: [https://www.kaggle.com/vitdegtyarev/ml-models-  
744 for-cellular-beams?scriptVersionId=63075739](https://www.kaggle.com/vitdegtyarev/ml-models-for-cellular-beams?scriptVersionId=63075739).

745 The developed ML models were explained and interpreted by evaluating the

746 relative feature importance using the permutations and SHAP methods. SHAP  
747 feature dependence was also determined and discussed. It was demonstrated  
748 that the beam span length, beam flange width, and beam web thickness are  
749 the most important features in predicting the elastic buckling by the developed  
750 models, with the opening end distance and beam height being the least im-  
751 portant parameters. The most important features in predicting the ultimate  
752 load are the beam span length, web post width, beam web thickness, and beam  
753 flange width. The opening end distance and opening diameter are the least  
754 important characteristics. These results align well with the mechanics-based  
755 knowledge demonstrating that the developed ML models can capture the web  
756 opening effects from the data used for their training. Contour plots of  $w_{cr}$  and  
757  $w_{max}$  predicted by the CatBoost model as functions of  $H/D_o$  and  $S_o/D_o$  were  
758 presented and discussed. For most beams,  $S_o/D_o$  affects  $w_{cr}$  and  $w_{max}$  more  
759 significantly than  $H/D_o$ , with  $S_o/D_o=1.3$  being the optimal value.

760 A web application for predicting the elastic buckling and ultimate loads was  
761 created in Streamlit. The lite version of the application has been deployed to  
762 the cloud at: <https://scba-cb.herokuapp.com/>. It can be opened and  
763 run in any web browser on any device, including mobile. The source codes  
764 of the full and lite application versions can be accessed on GitHub at <https://github.com/vitdegtyarev/SCBA-Streamlit> and <https://github.com/vitdegtyarev/SCBA-Streamlit-CB>, respectively.

767 The presented study demonstrates the opportunities for using ML methods  
768 for predicting the elastic buckling and ultimate loads of cellular beams. However,  
769 it should be noted that the developed models are based on the data for cellular  
770 beams with relatively short spans, not exceeding 8 m in the elastic buckling  
771 load dataset and 7 m in the ultimate load dataset. Therefore, the developed  
772 models are limited to beams with such spans. In modern construction, cellular

773 beams are often used for spans ranging from 9 to 18 m [103]. Future work  
774 should concentrate on extending the datasets to the beams with longer spans  
775 and retraining the ML models using the extended data. The reliability of the  
776 ultimate load predictions by the ML models should also be evaluated, and an  
777 appropriate safety factor determined.

## 778 **References**

- 779 [1] P. K. Das, S. L. Srimani, Handbook for the design of castellated beams,  
780 Central Mechanical Engineering Research Institute, Oxford & IBH Pub-  
781 lishing Company, New Delhi, Delhi, India, 1984.
- 782 [2] R. Lawson, S. Hicks, Design of composite beams with large web openings  
783 SCI P355, Steel Construction Institute, Berkshire, UK, 2011.
- 784 [3] M. I. M. H. Martini, Elasto-plastic lateral torsional buckling of steel  
785 beams with perforated web, Ph.D. thesis, United Arab Emirates Uni-  
786 versity (2011).
- 787 [4] A. M. Sweedan, Elastic lateral stability of I-shaped cellular steel beams,  
788 Journal of Constructional Steel Research 67 (2) (2011) 151–163. doi:  
789 10.1016/j.jcsr.2010.08.009.
- 790 [5] M. M. Sehwal, Lateral torsional buckling of steel i-section cellular beams,  
791 Ph.D. thesis, Eastern Mediterranean University (EMU)-Doğu Akdeniz  
792 Üniversitesi (DAÜ) (2013).
- 793 [6] D. Sonck, J. Belis, Lateral–torsional buckling resistance of cellular beams,  
794 Journal of Constructional Steel Research 105 (2015) 119–128. doi:10.1  
795 016/j.jcsr.2014.11.003.

- 796 [7] P. Panedpojaman, W. Sae-Long, T. Chub-uppakarn, Cellular beam design  
797 for resistance to inelastic lateral-torsional buckling, *Thin-Walled Structures* 99 (2016) 182–194. doi:10.1016/j.tws.2015.08.026.  
798
- 799 [8] F. P. V. Ferreira, A. Rossi, C. H. Martins, Lateral-torsional buckling of  
800 cellular beams according to the possible updating of EC3, *Journal of Con-*  
801 *structional Steel Research* 153 (2019) 222–242. doi:10.1016/j.jcsr.2  
802 018.10.011.
- 803 [9] K. D. Tsavdaridis, C. D’Mello, Web buckling study of the behaviour and  
804 strength of perforated steel beams with different novel web opening shapes,  
805 *Journal of Constructional Steel Research* 67 (10) (2011) 1605–1620. doi:  
806 10.1016/j.jcsr.2011.04.004.
- 807 [10] P. Panedpojaman, T. Thepchatri, S. Limkatanyu, Novel design equations  
808 for shear strength of local web-post buckling in cellular beams, *Thin-*  
809 *Walled Structures* 76 (2014) 92–104. doi:10.1016/j.tws.2013.11.007.
- 810 [11] L. F. Grilo, R. H. Fakury, G. de Souza Veríssimo, et al., Design procedure  
811 for the web-post buckling of steel cellular beams, *Journal of Constructional*  
812 *Steel Research* 148 (2018) 525–541. doi:10.1016/j.jcsr.2018.06.020.
- 813 [12] BS EN 1993-1-1: 2005. Design of steel structures–Part 1-1 General rules  
814 and rules for buildings, British Standards Institution, London, UK, 2005.
- 815 [13] ANSI/AISC 360-10. Specification for structural steel buildings, American  
816 Institute of Steel Construction, Chicago, Illinois, USA, 2010.
- 817 [14] K. F. Chung, T. Liu, A. Ko, Investigation on Vierendeel mechanism in  
818 steel beams with circular web openings, *Journal of Constructional Steel*  
819 *Research* 57 (5) (2001) 467–490. doi:10.1016/S0143-974X(00)00035-3.

- 820 [15] L. Kang, S. Hong, X. Liu, Shear behaviour and strength design of cellular  
821 beams with circular or elongated openings, *Thin-Walled Structures* 160  
822 (2021) 107353. doi:10.1016/j.tws.2020.107353.
- 823 [16] E. Ellobody, Nonlinear analysis of cellular steel beams under combined  
824 buckling modes, *Thin-Walled Structures* 52 (2012) 66–79. doi:10.1016/  
825 j.tws.2011.12.009.
- 826 [17] K. D. Tsavdaridis, C. D’Mello, Vierendeel bending study of perforated  
827 steel beams with various novel web opening shapes through nonlinear  
828 finite-element analyses, *Journal of Structural Engineering* 138 (10) (2012)  
829 1214–1230. doi:10.1061/(ASCE)ST.1943-541X.0000562.
- 830 [18] N. D. Lagaros, L. D. Psarras, M. Papadrakakis, G. Panagiotou, Optimum  
831 design of steel structures with web openings, *Engineering Structures* 30 (9)  
832 (2008) 2528–2537. doi:10.1016/j.engstruct.2008.02.002.
- 833 [19] K. Tsavdaridis, C. D’Mello, FE investigation of perforated sections with  
834 standard and non-standard web opening configurations and sizes, in: *The*  
835 *6th International Conference on Advances in Steel Structures (ICASS*  
836 *2009)*, 16-18 December 2009, pp. 213–220.
- 837 [20] F. Erdal, M. P. Saka, Ultimate load carrying capacity of optimally de-  
838 signed steel cellular beams, *Journal of Constructional Steel Research* 80  
839 (2013) 355–368. doi:10.1016/j.jcsr.2012.10.007.
- 840 [21] A. Jamadar, P. Kumbhar, Parametric study of castellated beam with  
841 circular and diamond shaped openings, *International Research Journal of*  
842 *Engineering and Technology* 2 (2) (2015) 715–722.
- 843 [22] K. D. Tsavdaridis, J. J. Kingman, V. V. Toropov, Application of structural

- 844 topology optimisation to perforated steel beams, *Computers & Structures*  
845 158 (2015) 108–123. doi:10.1016/j.compstruc.2015.05.004.
- 846 [23] S. G. Morkhade, L. M. Gupta, An experimental and parametric study  
847 on steel beams with web openings, *International Journal of Advanced*  
848 *Structural Engineering (IJASE)* 7 (3) (2015) 249–260. doi:10.1007/s4  
849 0091-015-0095-4.
- 850 [24] K. D. Tsavdaridis, G. Galiatsatos, Assessment of cellular beams with  
851 transverse stiffeners and closely spaced web openings, *Thin-Walled Struc-*  
852 *tures* 94 (2015) 636–650. doi:10.1016/j.tws.2015.05.005.
- 853 [25] V. Akrami, S. Erfani, Review and assessment of design methodologies for  
854 perforated steel beams, *Journal of Structural Engineering* 142 (2) (2016)  
855 04015148. doi:10.1061/(ASCE)ST.1943-541X.0001421.
- 856 [26] SEI/ASCE 23-97. Specifications for structural steel beams with web open-  
857 ings, American Society of Civil Engineers, Reston, VA, USA, 1999.
- 858 [27] J. Ward, Design of composite and non-composite cellular beams SCI P100,  
859 Steel Construction Institute, Berkshire, UK, 1990.
- 860 [28] K. F. Chung, C. Liu, A. Ko, Steel beams with large web openings of  
861 various shapes and sizes: an empirical design method using a generalised  
862 moment-shear interaction curve, *Journal of Constructional Steel Research*  
863 59 (9) (2003) 1177–1200. doi:10.1016/S0143-974X(03)00029-4.
- 864 [29] K. Rajana, K. D. Tsavdaridis, E. Koltsakis, Elastic and inelastic buckling  
865 of steel cellular beams under strong-axis bending, *Thin-Walled Structures*  
866 156 (2020) 106955. doi:10.1016/j.tws.2020.106955.
- 867 [30] F. Jiang, Y. Jiang, H. Zhi, Y. Dong, H. Li, S. Ma, Y. Wang, Q. Dong,  
868 H. Shen, Y. Wang, Artificial intelligence in healthcare: past, present and

- 869 future, *Stroke and Vascular Neurology* 2 (4). doi:10.1136/svn-2017-0  
870 00101.
- 871 [31] N. R. Tadapaneni, Artificial intelligence in finance and investments, *International Journal of Innovative Research in Science, Engineering and*  
872 *Technology* 9 (5) (2019) 2792–2795.
- 874 [32] Y. Ma, Z. Wang, H. Yang, L. Yang, Artificial intelligence applications in  
875 the development of autonomous vehicles: a survey, *IEEE/CAA Journal*  
876 *of Automatica Sinica* 7 (2) (2020) 315–329. doi:10.1109/JAS.2020.100  
877 3021.
- 878 [33] T. Wuest, D. Weimer, C. Irgens, K.-D. Thoben, Machine learning in man-  
879 ufacturing: advantages, challenges, and applications, *Production & Man-*  
880 *ufacturing Research* 4 (1) (2016) 23–45. doi:10.1080/21693277.2016.  
881 1192517.
- 882 [34] N. Kartam, I. Flood, J. H. Garrett, *Artificial Neural Networks for Civil*  
883 *Engineers: Fundamentals and Applications*, American Society of Civil  
884 Engineers, 1997.
- 885 [35] H. Adeli, Neural networks in civil engineering: 1989–2000, *Computer-*  
886 *Aided Civil and Infrastructure Engineering* 16 (2) (2001) 126–142. doi:  
887 10.1111/0885-9507.00219.
- 888 [36] H. Salehi, R. Burgueño, Emerging artificial intelligence methods in struc-  
889 tural engineering, *Engineering Structures* 171 (2018) 170–189. doi:  
890 10.1016/j.engstruct.2018.05.084.
- 891 [37] H. Sun, H. V. Burton, H. Huang, Machine learning applications for build-  
892 ing structural design and performance assessment: state-of-the-art review,

- 893 Journal of Building Engineering (2020) 101816doi:10.1016/j.jobe.202  
894 0.101816.
- 895 [38] M. Z. Naser, Systematic Integration of Artificial Intelligence Toward Eval-  
896 uating Response of Materials and Structures in Extreme Conditions,  
897 Springer Transactions in Civil and Environmental Engineering, Springer,  
898 2021, p. 183–212. doi:10.1007/978-981-15-5772-9\_10.
- 899 [39] M. Naser, Mechanistically informed machine learning and artificial in-  
900 telligence in fire engineering and sciences, Fire Technology (2021) 1–  
901 44doi:10.1007/s10694-020-01069-8.
- 902 [40] H.-T. Thai, Machine learning for structural engineering: A state-of-the-art  
903 review, Structures (2022) 448–491doi:10.1016/j.istruc.2022.02.003.
- 904 [41] A. Çevik, A. E. Kurtoğlu, M. Bilgehan, M. E. Gülşan, H. M. Albegmprli,  
905 Support vector machines in structural engineering: a review, Journal of  
906 Civil Engineering and Management 21 (3) (2015) 261–281. doi:10.384  
907 6/13923730.2015.1005021.
- 908 [42] C. Liu, C. Liu, C. Liu, X. Huang, J. Miao, W. Xu, Fire damage identifi-  
909 cation in RC beams based on support vector machines considering vibra-  
910 tion test, KSCE Journal of Civil Engineering 23 (10) (2019) 4407–4416.  
911 doi:10.1007/s12205-019-2353-7.
- 912 [43] J. Zhang, G. Ma, Y. Huang, F. Aslani, B. Nener, et al., Modelling uniaxial  
913 compressive strength of lightweight self-compacting concrete using random  
914 forest regression, Construction and Building Materials 210 (2019) 713–719.  
915 doi:10.1016/j.conbuildmat.2019.03.189.
- 916 [44] S. Mangalathu, S.-H. Hwang, J.-S. Jeon, Failure mode and effects analy-  
917 sis of rc members based on machine-learning-based shapley additive ex-

- 918 planations (SHAP) approach, *Engineering Structures* 219 (2020) 110927.  
919 doi:10.1016/j.engstruct.2020.110927.
- 920 [45] R. Solhmirzaei, H. Salehi, V. Kodur, M. Naser, Machine learning frame-  
921 work for predicting failure mode and shear capacity of ultra high per-  
922 formance concrete beams, *Engineering Structures* 224 (2020) 111221.  
923 doi:10.1016/j.engstruct.2020.111221.
- 924 [46] M. S. Ahmad, S. M. Adnan, S. Zaidi, P. Bhargava, A novel support vector  
925 regression (SVR) model for the prediction of splice strength of the uncon-  
926 fined beam specimens, *Construction and Building Materials* 248 (2020)  
927 118475. doi:10.1016/j.conbuildmat.2020.118475.
- 928 [47] S. Mangalathu, H. Jang, S.-H. Hwang, J.-S. Jeon, Data-driven machine-  
929 learning-based seismic failure mode identification of reinforced concrete  
930 shear walls, *Engineering Structures* 208 (2020) 110331. doi:10.1016/j.  
931 engstruct.2020.110331.
- 932 [48] M. Naser, H. Salehi, Machine learning-driven assessment of fire-induced  
933 concrete spalling of columns, *ACI Materials Journal* 117 (6) (2020) 7–16.  
934 doi:10.14359/51728120.
- 935 [49] D.-C. Feng, Z.-T. Liu, X.-D. Wang, Y. Chen, J.-Q. Chang, D.-F. Wei,  
936 Z.-M. Jiang, Machine learning-based compressive strength prediction for  
937 concrete: An adaptive boosting approach, *Construction and Building Ma-  
938 terials* 230 (2020) 117000. doi:10.1016/j.conbuildmat.2019.117000.
- 939 [50] T. Nguyen-Sy, J. Wakim, Q.-D. To, M.-N. Vu, T.-D. Nguyen, T.-T.  
940 Nguyen, Predicting the compressive strength of concrete from its compo-  
941 sitions and age using the extreme gradient boosting method, *Construction  
942 and Building Materials* 260 (2020) 119757. doi:10.1016/j.conbuildma  
943 t.2020.119757.

- 944 [51] M. R. Kaloop, D. Kumar, P. Samui, J. W. Hu, D. Kim, Compressive  
945 strength prediction of high-performance concrete using gradient  
946 tree boosting machine, *Construction and Building Materials* 264 (2020)  
947 120198. doi:10.1016/j.conbuildmat.2020.120198.
- 948 [52] A. Marani, M. L. Nehdi, Machine learning prediction of compressive  
949 strength for phase change materials integrated cementitious composites,  
950 *Construction and Building Materials* 265 (2020) 120286. doi:10.1016/  
951 j.conbuildmat.2020.120286.
- 952 [53] W. B. Chaabene, M. Flah, M. L. Nehdi, Machine learning prediction  
953 of mechanical properties of concrete: Critical review, *Construction and*  
954 *Building Materials* 260 (2020) 119889. doi:10.1016/j.conbuildmat.20  
955 20.119889.
- 956 [54] H. Nguyen, T. Vu, T. P. Vo, H.-T. Thai, Efficient machine learning models  
957 for prediction of concrete strengths, *Construction and Building Materials*  
958 266 (2021) 120950. doi:10.1016/j.conbuildmat.2020.120950.
- 959 [55] M.-C. Kang, D.-Y. Yoo, R. Gupta, Machine learning-based prediction  
960 for compressive and flexural strengths of steel fiber-reinforced concrete,  
961 *Construction and Building Materials* 266 (2021) 121117. doi:10.1016/  
962 j.conbuildmat.2020.121117.
- 963 [56] M. Su, Q. Zhong, H. Peng, S. Li, Selected machine learning approaches  
964 for predicting the interfacial bond strength between FRPs and concrete,  
965 *Construction and Building Materials* 270 (2021) 121456. doi:10.1016/  
966 j.conbuildmat.2020.121456.
- 967 [57] O. B. Olalusi, P. O. Awoyera, Shear capacity prediction of slender rein-  
968 forced concrete structures with steel fibers using machine learning, *Engi-*

- 969           neering Structures 227 (2021) 111470. doi:10.1016/j.engstruct.2020  
970           .111470.
- 971 [58] H. D. Nguyen, G. T. Truong, M. Shin, Development of extreme gradient  
972           boosting model for prediction of punching shear resistance of r/c interior  
973           slabs, Engineering Structures 235 (2021) 112067. doi:10.1016/j.engstr  
974           uct.2021.112067.
- 975 [59] D.-C. Feng, W.-J. Wang, S. Mangalathu, G. Hu, T. Wu, Implement-  
976           ing ensemble learning methods to predict the shear strength of RC  
977           deep beams with/without web reinforcements, Engineering Structures 235  
978           (2021) 111979. doi:10.1016/j.engstruct.2021.111979.
- 979 [60] J. Rahman, K. S. Ahmed, N. I. Khan, K. Islam, S. Mangalathu, Data-  
980           driven shear strength prediction of steel fiber reinforced concrete beams us-  
981           ing machine learning approach, Engineering Structures 233 (2021) 111743.  
982           doi:10.1016/j.engstruct.2020.111743.
- 983 [61] D.-C. Feng, B. Cetiner, M. R. Azadi Kakavand, E. Taciroglu, Data-driven  
984           approach to predict the plastic hinge length of reinforced concrete columns  
985           and its application, Journal of Structural Engineering 147 (2) (2021)  
986           04020332. doi:10.1061/(ASCE)ST.1943-541X.0002852.
- 987 [62] S. Mangalathu, H. Shin, E. Choi, J.-S. Jeon, Explainable machine learning  
988           models for punching shear strength estimation of flat slabs without trans-  
989           verse reinforcement, Journal of Building Engineering 39 (2021) 102300.  
990           doi:10.1016/j.jobe.2021.102300.
- 991 [63] S.-H. Hwang, S. Mangalathu, J. Shin, J.-S. Jeon, Machine learning-based  
992           approaches for seismic demand and collapse of ductile reinforced concrete  
993           building frames, Journal of Building Engineering 34 (2021) 101905. doi:  
994           10.1016/j.jobe.2020.101905.

- 995 [64] B. Fu, D.-C. Feng, A machine learning-based time-dependent shear  
996 strength model for corroded reinforced concrete beams, *Journal of Build-  
997 ing Engineering* 36 (2021) 102118. doi:10.1016/j.jobbe.2020.102118.
- 998 [65] Z. Liu, A. Guo, Empirical-based support vector machine method for  
999 seismic assessment and simulation of reinforced concrete columns us-  
1000 ing historical cyclic tests, *Engineering Structures* 237 (2021) 112141.  
1001 doi:10.1016/j.engstruct.2021.112141.
- 1002 [66] V. V. Degtyarev, Machine learning models for predicting bond strength  
1003 of deformed bars in concrete, *ACI Structural Journal* (in press).
- 1004 [67] M. Kumar, N. Yadav, Buckling analysis of a beam-column using multi-  
1005 layer perceptron neural network technique, *Journal of the Franklin Insti-  
1006 tute* 350 (10) (2013) 3188–3204. doi:10.1016/j.jfranklin.2013.07.  
1007 016.
- 1008 [68] A. Tashakori, H. Adeli, Optimum design of cold-formed steel space struc-  
1009 tures using neural dynamics model, *Journal of Constructional Steel Re-  
1010 search* 58 (2002) 1545–1566. doi:10.1016/S0143-974X(01)00105-5.
- 1011 [69] I. H. Guzelbey, A. Cevik, A. Erklig, Prediction of web crippling strength  
1012 of cold-formed steel sheetings using neural networks, *Journal of Construc-  
1013 tional Steel Research* 62 (10) (2006) 962–973. doi:10.1016/j.jcsr.200  
1014 6.01.008.
- 1015 [70] M. Pala, A new formulation for distortional buckling stress in cold-formed  
1016 steel members, *Journal of Constructional Steel Research* 62 (7) (2006)  
1017 716–722. doi:10.1016/j.jcsr.2005.09.011.
- 1018 [71] M. Pala, N. Caglar, A parametric study for distortional buckling stress on

- 1019 cold-formed steel using a neural network, *Journal of Constructional Steel*  
1020 *Research* 63 (5) (2007) 686–691. doi:10.1016/j.jcsr.2006.07.005.
- 1021 [72] M. D’Aniello, E. M. Güneyisi, R. Landolfo, K. Mermerdaş, Analytical  
1022 prediction of available rotation capacity of cold-formed rectangular and  
1023 square hollow section beams, *Thin-Walled Structures* 77 (2014) 141–152.  
1024 doi:10.1016/j.tws.2013.09.015.
- 1025 [73] S. Lee, T. P. Vo, H.-T. Thai, J. Lee, V. Patel, Strength prediction of  
1026 concrete-filled steel tubular columns using Categorical Gradient Boosting  
1027 algorithm, *Engineering Structures* 238 (2021) 112109. doi:10.1016/j.  
1028 engstruct.2021.112109.
- 1029 [74] M. A. B. Kabir, A. S. Hasan, A. M. Billah, Failure mode identification  
1030 of column base plate connection using data-driven machine learning tech-  
1031 niques, *Engineering Structures* 240 (2021) 112389. doi:10.1016/j.eng  
1032 struct.2021.112389.
- 1033 [75] Y. Xu, B. Zheng, M. Zhang, Capacity prediction of cold-formed stainless  
1034 steel tubular columns using machine learning methods, *Journal of Con-  
1035 structional Steel Research* 182 (2021) 106682. doi:10.1016/j.jcsr.202  
1036 1.106682.
- 1037 [76] X. Guan, H. Burton, M. Shokrabadi, Z. Yi, Seismic drift demand esti-  
1038 mation for steel moment frame buildings: From mechanics-based to data-  
1039 driven models, *Journal of Structural Engineering* 147 (6) (2021) 04021058.  
1040 doi:10.1061/(ASCE)ST.1943-541X.0003004.
- 1041 [77] V. V. Degtyarev, Neural networks for predicting shear strength of CFS  
1042 channels with slotted webs, *Journal of Constructional Steel Research* 177  
1043 (2021) 106443. doi:10.1016/j.jcsr.2020.106443.

- 1044 [78] V. V. Degtyarev, M. Z. Naser, Boosting machines for predicting shear  
1045 strength of CFS channels with staggered web perforations, Structures 34  
1046 (2021) 3391–3403. doi:10.1016/j.istruc.2021.09.060.
- 1047 [79] M. Z. Naser, V. Kodur, H.-T. Thai, R. Hawileh, J. Abdalla, V. V. Degt-  
1048 yarev, Structuresnet and firenet: Benchmarking databases and machine  
1049 learning algorithms in structural and fire engineering domains, Journal of  
1050 Building Engineering 44 (2021) 102977. doi:10.1016/j.jobbe.2021.10  
1051 297.
- 1052 [80] V. V. Degtyarev, Predicting shear strength of cfs channels with slotted  
1053 webs by machine learning models, Architecture, Structures and Construc-  
1054 tiondoi:10.1007/s44150-021-00001-0.
- 1055 [81] Y. Sharifi, A. Moghbeli, M. Hosseinpour, H. Sharifi, Neural networks for  
1056 lateral torsional buckling strength assessment of cellular steel I-beams,  
1057 Advances in Structural Engineering 22 (9) (2019) 2192–2202. doi:10.1  
1058 177/1369433219836176.
- 1059 [82] AS 4100:1990. Steel structures, Standards Association of Australia, Syd-  
1060 ney, Australia, 1990.
- 1061 [83] M. Abambres, K. Rajana, K. D. Tsavdaridis, T. P. Ribeiro, Neural  
1062 network-based formula for the buckling load prediction of I-section cellular  
1063 steel beams, Computers 8 (1) (2019) 2. doi:10.3390/computers8010002.
- 1064 [84] F. P. V. Ferreira, R. Shamass, V. Limbachiya, K. D. Tsavdaridis, C. H.  
1065 Martins, Lateral-torsional buckling resistance prediction model for steel  
1066 cellular beams generated by Artificial Neural Networks (ANN), Thin-  
1067 Walled Structures 170 (2022) 108592. doi:10.1016/j.tws.2021.108592.
- 1068 [85] V. Limbachiya, R. Shamass, Application of artificial neural networks for

- 1069 web-post shear resistance of cellular steel beams, *Thin-Walled Structures*  
1070 161 (2021) 107414. doi:doi.org/10.1016/j.tws.2020.107414.
- 1071 [86] S. Lundberg, S.-I. Lee, A unified approach to interpreting model predic-  
1072 tions, arXiv preprint arXiv:1705.07874.
- 1073 [87] S. Fares, J. Coulson, D. Dinehart, *Design Guide 31: Castellated and Cel-  
1074 lular Beam Design*, American Institute of Steel Construction, Chicago, IL,  
1075 USA, 2016.
- 1076 [88] T. Hastie, R. Tibshirani, J. Friedman, *The elements of statistical learn-  
1077 ing: data mining, inference, and prediction*, Springer Science & Business  
1078 Media, 2009.
- 1079 [89] A. Géron, *Hands-on machine learning with Scikit-Learn, Keras, and Ten-  
1080 sorFlow: Concepts, tools, and techniques to build intelligent systems*,  
1081 O'Reilly Media, 2019.
- 1082 [90] L. Breiman, Random forests, *Machine learning* 45 (1) (2001) 5–32. doi:  
1083 10.1023/A:1010933404324.
- 1084 [91] T. K. Ho, Random decision forests, in: *Proceedings of 3rd international  
1085 conference on document analysis and recognition*, Vol. 1, IEEE, 1995, pp.  
1086 278–282. doi:10.1109/ICDAR.1995.598994.
- 1087 [92] J. H. Friedman, Greedy function approximation: a gradient boosting ma-  
1088 chine, *Annals of Statistics* (2001) 1189–1232.
- 1089 [93] F. Pedregosa, G. Varoquaux, A. Gramfort, V. Michel, B. Thirion,  
1090 O. Grisel, M. Blondel, P. Prettenhofer, R. Weiss, V. Dubourg, et al.,  
1091 *Scikit-learn: Machine learning in Python*, the *Journal of Machine Learn-  
1092 ing Research* 12 (2011) 2825–2830.

- 1093 [94] T. Chen, C. Guestrin, XGBoost: A scalable tree boosting system, in:  
1094 Proceedings of the 22nd acm sigkdd international conference on knowledge  
1095 discovery and data mining, 2016, pp. 785–794. doi:10.1145/2939672.  
1096 2939785.
- 1097 [95] G. Ke, Q. Meng, T. Finley, T. Wang, W. Chen, W. Ma, Q. Ye, T.-Y. Liu,  
1098 LightGBM: A highly efficient gradient boosting decision tree, Advances  
1099 in Neural Information Processing Systems 30 (2017) 3146–3154.
- 1100 [96] A. V. Dorogush, V. Ershov, A. Gulin, CatBoost: gradient boosting with  
1101 categorical features support, arXiv preprint arXiv:1810.11363.
- 1102 [97] M. Naser, A. Alavi, Insights into performance fitness and error metrics for  
1103 machine learning, arXiv preprint arXiv:2006.00887.
- 1104 [98] M. Z. Naser, An engineer’s guide to eXplainable Artificial Intelligence and  
1105 Interpretable Machine Learning: Navigating causality, forced goodness,  
1106 and the false perception of inference, Automation in Construction 129  
1107 (2021) 103821. doi:10.1016/j.autcon.2021.103821.
- 1108 [99] B. Peleg, P. Sudhölter, Introduction to the theory of cooperative games,  
1109 Vol. 34, Springer Science & Business Media, 2007.
- 1110 [100] BS EN 1993-1-5: 2006. Design of steel structures–Part 1-5 Plated struc-  
1111 tural elements, British Standards Institution, London, UK, 2006.
- 1112 [101] ANSI/AISC 360-16. Specification for structural steel buildings, American  
1113 Institute of Steel Construction, Chicago, Illinois, USA, 2016.
- 1114 [102] C. Topkaya, S. Şahin, A comparative study of AISC-360 and EC3 strength  
1115 limit states, International Journal of Steel Structures 11 (1) (2011) 13–27.  
1116 doi:10.1007/S13296-011-1002-x.

1117 [103] S. J. Hicks, R. M. Lawson, J. W. Rackham, P. Fordham, Comparative  
1118 structure cost of modern commercial buildings, Steel Construction Insti-  
1119 tute, 2004.